Thesis for The Degree of Doctor of Philosophy

Thermoplastic arabinoxylan derivatives

A study of their structure and dynamics

Ratchawit Janewithayapun

Department of Chemistry and Chemical Engineering
Chalmers University of Technology
Gothenburg, Sweden, 2025

Thermoplastic arabinoxylan derivatives
A study of their structure and dynamics

Ratchawit Janewithayapun

ISBN 978-91-8103-316-8

Acknowledgements, dedications, and similar personal statements in this thesis, reflect the author's own views.

Doktorsavhandlingar vid Chalmers tekniska högskola
Ny serie nr 5773
ISSN 0346-718X
https://doi.org/10.63959/chalmers.dt/5773

Department of Chemistry and Chemical Engineering
Chalmers University of Technology
SE-412 96 Göteborg,
Sweden
Phone: +46(0)31 772 1000

Cover page showing wheat plants with the nothern lights overhead, representing the material and the synchrotron, neutron and NMR techniques used to probe them in this work. Art by Juntima Nawilaijaroen

Printed by Chalmers Digitaltryck,
Gothenburg, Sweden 2025.

Thermoplastic arabinoxylan derivatives
A study of their structure and dynamics

Ratchawit Janewithayapun

Department of Chemistry and Chemical Engineering
Chalmers University of Technology

Abstract

The structure and dynamics of polymers at the molecular and nanometer scale controls how the material responds to stimuli such as heat and strain. To advance the development of polysaccharide-based thermoplastics require that we also further our understanding of their molecular scale properties and how these are altered by modification processes. This thesis aims to understand the mechanisms that allow for a flexible thermoplastic polysaccharide material to be produced via oxidation-reduction and etherification modification of arabinoxylan (AX). The effect of these modifications on the structure and dynamics of linear polysaccharides, such as cellulose and alginate, have been studied but with few experimental measurements of changes at the molecular scale. Characterization of modifications on branched polysaccharides such as AX are even more limited.

AX studied in this work, is a polysaccharide consisting of β-(1→4)-D-xylopyranosyl repeating units partially substituted with α-*L*-arabinofuranosyl units, and is a major hemicellulose component in wheat bran. To understand the changes in structure, we utilize small and wide-angle X-ray scattering techniques to characterize solid films and water dispersions. To study the dynamics, we combine thermomechanical characterization, NMR and quasielastic neutron scattering techniques to obtain information across different timescales.

A higher degree of arabinose substitution in AX was correlated with a more extended chain conformation when dispersed in water, and the absence of ordered crystalline regions in the solid films. Oxidation-reduction that results in the ring-opening of the AX does not significantly alter the conformation in water, however, increased chain mobility was observed in the ring-opened solid materials, specifically at the modified positions of the carbohydrate ring. Etherification leads to nanoscale phase separation in the system's structure, and adds sub-glass transitions to the dynamics. Lastly, when combining oxidation-reduction with etherification, we observed synergistic effects from the mobility of the ring-opened AX chain and the additional motions provided by the side chains.

Keywords

Polysaccharide, hemicellulose, small-angle scattering, solid-state NMR, polymer conformation, quasielastic neutron scattering

List of Publications

This thesis is based on the following publications and manuscripts:

1. **R. Janewithayapun**, F. Cousin, P. F. M. Pereira, F. Herranz-Trillo, A. E. Terry, J. S. Pedersen, A. J. Quero, A. Ström, *Correlation between arabinose content and the conformation of arabinoxylan in water dispersions, Carbohydrate Polymers 368, 124082*

2. **R. Janewithayapun**, H. Karlsson, F. Herranz-Trillo, A. E. Terry, L. Evenäs, F. Cousin, A. Ström, *Effect of periodate oxidation and borohydride reduction on the chemical structure and chain conformation of arabinoxylan, Submitted to Carbohydrate Polymers*

3. **R. Janewithayapun**, H. Karlsson, M. S. Hedenqvist, D. W. Juhl, T. Vosegaard, L. Evenäs, A. Ström, *Dynamics of ring-opened arabinoxylan studied with solid-state NMR, Manuscript*

4. **R. Janewithayapun**, M. S. Hedenqvist, F. Cousin, A. Idström, L. Evenäs, P. Lopez-Sanchez, G. Westman, A. Larsson, A. Ström, *Nanostructures of etherified arabinoxylans and the effect of arabinose content on material properties, Carbohydrate Polymers 331, 121846*

Other publications

The following publications were published during my PhD studies, or are currently in submission/under revision. However, they are not appended to this thesis, as the contents are not directly related to the thesis.

[**a**] S. L.Navarro, E. Orzan, **R. Janewithayapun**, P. Penttilä, A. Ström, R. Kádár, T. Nypelö, *Tert-butanol as a structuring agent for cellulose nanocrystal fluids and foams, Biomacromolecules 2025, 26, 9, 5591–5600*

[**b**] C. Palasingh, **R. Janewithayapun**, L. P. Cavalcanti, F. Abik, K. S. Mikkonen, F. Cousin, A. Ström, T. Nypelö, *Aggregation of modified glucuronoxylan in water and DMSO, Manuscript*

[**c**] C. Rämgård, M. L. Parada, **R. Janewithayapun**, T. V. Vuong, E. R. Master, A. Ström, L. S. McKee, F. Vilaplana, *Tuning the Rheological Properties of Laccase-Crosslinked Arabinoxylan Hydrogels by Prior Arabinofuranosidase Treatments, Food Hydrocolloids (October 2025), 112080*

Contributions to the publications

Paper I: I extracted arabinoxylan, prepared the samples and was involved in collecting and processing of SAXS data, which I analyzed and fitted. I also performed size-exclusion chromatography and monosaccharide composition analysis. I wrote the original draft and made subsequent edits of the manuscript.

Paper II: I designed the study, applied for beamtime and planned experiments. I prepared and synthesized samples, and was involved in SAXS data collection, processing and fitting. I interpreted NMR data collected from the Swedish NMR centre. I wrote the original draft and made subsequent edits of the manuscript.

Paper III: I designed the study and applied for NMR experimental time. I prepared the samples and interpreted the solid-state NMR data. I wrote the original draft and made subsequent edits of the manuscript.

Paper IV: I extracted arabinoxylan, synthesized the derivatives and performed all measurements except for DOSY NMR. I wrote the original draft and made subsequent edits of the manuscript.

Acknowledgments

As this eventful and wondrous chapter comes to an end, I would like to acknowledge my family, friends, colleagues and supervisors who have been a part of this journey, and have invaluably enriched the experience. Thank you! I will definitely bring with me the joyous atmosphere that have uplifted the good times and blunted the tough ones.

To my PhD supervisor Anna, I express my heartfelt gratitude for all the guidance and discussions throughout the years. Most of all, thank you encouraging me to try out my ideas and experiments, even when it meant having to join me on four beamtimes in the span of a month. These endeavours could not have begun without your support and openness for discussions. Hopefully we will still have the chance to collaborate on some more of those in the future! I would like to thank all of my co-supervisors as well; to Fabrice, thank you for introducing me to the field of small-angle scattering, which has become a core part of this thesis, and for showing me around during my visits to France. To Mikael, thank you for your help with measuring and interpreting polymer dynamics, and for taking up the driver's mantle during our beamtime in the UK. To Anette, thank you for introducing me to the FibRe research centre and for being there to make things happen whenever I needed a helping hand. A key person who is not a co-supervisor but has contributed so much to my work is Lasse; thank you very much for all your guidance on NMR matters. I will try my best to come back for my remaining credits in the NMR course. I would also like to thank my examiner Merima for checking on my progress during the PhD with care, and for your insightful feedback on the thesis draft.

I would like to acknowledge the collaborators who have contributed to make the work in this thesis possible. I extend a special thanks to Hampus from the FibRe research centre, Amparo and Pamela from Chalmers, Jan Skov from Aarhus University, and to Ann and Fatima from MAX IV. I am greatly thankful to the coauthors, instrument scientists (Mona, Markus, Quentin and Jean-Marc) and to everyone else who gave insightful input and feedback on the manuscripts, proposals and experiments.

It has been my privilege to be surrounded by amazing friends and colleagues both within Chalmers and outside. My officemates both past and present: Vishnu, Gain, Ehsan, Nive, Jakob and Giovanni, I really want to thank you for making the office such a pleasant space! To the latter two, I have kind of

given up trying to categorize you so I will thank you here for being wonderful friends, group members and officemates (maybe not Giovanni on this last one on account of his table drumming). To Saül, Bahiru and Mathias, it has been a pleasure working with you in the group, and to Maria, I'm sure you will have an amazing time working with Anna and the others. Without a doubt, having friends around at the division has made time fly faster: Maja, Mike, Eva, Giannis, Nicole, Alex, Jesper, Monika, Moa, Smaragda and Guido. I have had many fun lunchtime discussions, climbing sessions, afterworks and DnD campaigns with you all, in different combinations, thank you! I would also like to acknowledge the other members of the Anna/Anette/Merima extended group such as Åke, Arvindh, Luigi, Linus, Lucas and Carolina for the discussions and informations we have shared during the meetings, and to raise a cheer for our dear neighbours on the eighth floor Alex, Mavi, Krysztof, Mathis and others. I have also received a lot of help from our permanent staffs and researchers: Lotta, Anna, Emma, Mats, Sara and Andreas, who helped ensure everything in the division is functioning smoothly. The FibRe research centre, through the NextGen network and discussions with different PIs and projects has been a constant source of inspiration during the PhD. Lastly, I would like to thank all my other friends and colleagues who have been a part of my chapter here.

It has been a surprisingly long time since I arrived to Göteborg, and I was definitely a little bit lost back then. Fortunately, I met the kind and amazing people from the Thai Chalmers alumni community such as Jaa, Mick, Mono, Peach, Heart, Erng, Eve, Pun, Mimmy and Yod early on, who are still great friends today. Also quite early on in my studies, I met some of my best friends Christian and Eliott, who also happens to be my oldest collaborator to date. I really wonder if our knack for ending up in the same work place will keep on going. A bit later on, the group grew from shared hobbies of discgolf, boardgames, and grilling. To Viktor, Anton, Albin and the discgolf group, I hope our summer roadtrips keep being a tradition! And I remember that I should keep my promise to Anton and Anna to invite them for dinner and gossip. If Petter is reading, then I would also say to the group that I am looking forward to attempting to defend my Mecatol crown the next time we play.

My final words of thanks goes to my parents and family back home. Without your support early on, I would not have had the opportunity to choose so freely what I wanted to do. Thank you for the unending love and support, and for checking in by phone so that I don't forget how to speak Thai. I haven't managed to visit as often as I would have liked but hopefully there will be more chances soon!

Abbreviations and symbols

ASL	Acid soluble lignin
Ara$f$	Arabinofuranose
AX	Arabinoxylan
A/X ratio	Arabinose:xylose ratio
A_2	Second virial coefficient
BGE	Butyl glycidyl ether
CP	Cross-polarization
CP/MAS	Cross-polarization with magic-angle spinning
DAX	Dialdehyde arabinoxylan
DiolAX	Dialcohol arabinoxylan
DMA	Dynamic mechanical analysis
DO	Degree of oxidation (%)
DS	Degree of substitution
FWS	Fixed window scan
HPAEC	High-performance anion-exchange chromatography
L_p	Persistence length
M_w	Weight averaged molar mass
NMR	Nuclear magnetic resonance
q	Scattering vector, also momentum transfer
QENS	Quasielastic neutron scattering
R_g	Radius of gyration
SAXS	Small-angle X-ray scattering
SANS	Small-angle neutron scattering
SEC-MALS	Size exclusion chromatography with multi-angle light scattering
TFA	Trifluoracetic acid
$T_{1\rho\mathrm{H}}$	Proton relaxation time in the rotating frame
T_CH	Cross-polarization time constant
T_g	Glass transition temperature
WAXS	Wide-angle X-ray scattering
WISE	Wideline-separation
XRD	X-ray diffraction
Xyl$p$	Xylopyranose
ν	Flory exponent

Contents

Part I

Summary

Chapter 1

Introduction

Arabinoxylans (AX) are a subtype of xylan-based polysaccharides, with a backbone of β-(1→4)-D-xylopyranosyl units, partially substituted by α-*L*-arabinofuranosyl units on O-3 and/or O-2 of the xylose units [1]. AX constitutes the main hemicellulose component in cereals such as wheat, rye, barley and rice [2]. Wheat being a particularly essential agriculture plant, with global production of 808 million tonnes in 2025 [3], of which around 15 % w/w is wheat bran. The content of AX in wheat bran is between 10 - 30 % w/w [4–7], and as bran is typically removed prior to consumption, wheat bran is a major side-stream of the agricultural industry, thus making AX a viable source of natural polymers.

Processing and manufacturing of components from fossil fuel-based polymers involves significant softening of the polymers by heat and shear, i.e. melt-processing. As with most natural polymers, AX cannot be melt-processed in its native state due to their decomposition temperature being lower than their glass transition temperature (T_g) or melting temperature [8, 9]. Additional modifications or treatment of the natural polymers are required to overcome this gap between decomposition and softening temperatures, with chemical modification being one of the main approaches.

Through a sequence of oxidation-reduction-etherification reactions, it has been shown that a thermoplastic modified AX could be produced with compression moldability at 140 °C, and ductility above 100 % strain [8, 10]. Interestingly, similar melt-processability and ductility could not be obtained with only an etherification of AX [8, 10], or requires a larger degree of etherification or esterification of the polysaccharide materials [11]. Therefore, questions remain on the exact role and contributions of each modification step in the achieved thermoplasticity. On one hand, tuning or improvement of polysaccharide material mechanical properties, such as by controlling the extent of the oxidation-reduction, could be useful for applications. But also, if any of the modification steps could be optimized or removed, the energy and resource efficiency of the production process could be significantly improved.

In the context given above, the research questions investigated in this thesis are as follows:

1: Do different composition of AX materials, hence starting material properties influence those of the modified material? Here, the hypothesis is that different AX, with their variety of branching degrees behave differently and will impact the properties of the modified materials. (Papers I and IV)

2: How does oxidation-reduction and etherification affect the structure of AX at the atomic to nanometer length scale, and what roles do these structural changes have on the material properties? The hypothesis is that oxidation-reduction of AX chain reduces the persistence length of AX. Subsequent etherification introduces mobile segments or domains to the modified materials which may further alter the nanostructure. (Papers I, II and IV)

3: Do the modification steps above change the molecular dynamics of the AX material, and what are the mechanisms behind these changes? The hypothesis being that oxidation-reduction and etherification increases molecular motion in the modified AX material, which contributes to their improved macromolecular thermo-mechanical properties. (Papers III and IV)

Chapter 2

Background

This chapter presents a background of the materials, modifications, and relevant theoretical aspects of the methods used in this thesis.

2.1 Arabinoxylan

As mentioned in the introduction, the AX content in wheat bran is high, between 10 - 30 % w/w, comparable to for example, the cellulose content (10 % w/w) [7, 12]. AX constitutes of a xylan backbone (β-(1→4)-D-xylopyranosyl units) [13], with partial substitution of α-*L*-arabinofuranosyl units on the *O*-3 and/or *O*-2 of xylose units. In wheat AX, mono-substitution occurs primarily on the *O*-3 and *O*-2 substitution is typically only found when the xylose unit is di-substituted on both *O-3* and O-2 [14, 15]. Other substituents such as glucuronic acids, ferulic acid and other monosaccharides such as galactose may also be present in smaller amounts [2, 14]. Ferulic acid content is however low for alkali extracted AX, owing to cleavage of the ester bond [16]. Figures 2.1a-b show the symbol representation and the chemical structure of AX, respectively.

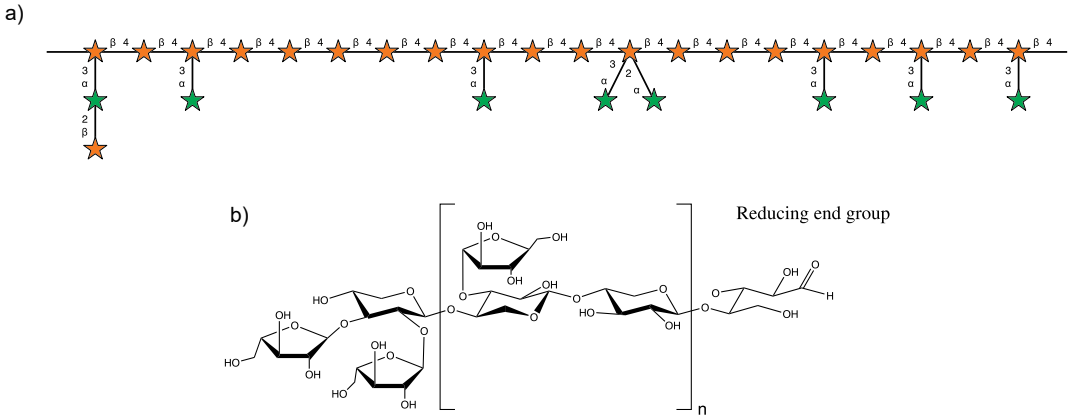

Figure 2.1: a) IUPAC symbol representation of AX. Arabinose groups (green star) are substituted onto a xylan backbone (orange stars), and b) chemical structure representation of AX (aliphatic protons not shown).

The subtitution pattern, in terms of the amount of arabinose, other side-groups, and the complexity of the substitution patterns vary depending on the location or layer of wheat bran [14]. For example, the outer beeswing layer of bran contains an arabinose to xylose ratio (A/X) of ~ 1 [17], while the more inner aleurone layer has a lower A/X of ~ 0.3 [18]. The lower A/X fractions has been shown to consist mainly of arabinose substitutions on *O*-3 of the xylose units. The substitution pattern of the higher A/X fractions can be more complex, consisting of both mono- and di-substitutions. Furthermore, larger content of non-terminal arabinose and xylose residues have been measured, meaning that dimeric substitutions of arabinose, xylose and other sugars occur [14].

As a result of the variations in substitution in AX, the water solubility of AX can vary between high solubility to near insolubility [19–21], furthermore, there have been discussions that the chain conformation in water may vary as well [20–22]. Debate still remain, however, on the extent of variation of the conformation with A/X [15, 23], perhaps due to the challenges in determining the chain conformation parameters, whether with light scattering [24] or with X-ray/neutron scattering [25]. In the solid form, the A/X ratio has been shown to affect the mechanical properties of AX films [26, 27], as AX can form ordered regions at lower A/X due to intermolecular interactions of the xylan backbone [27].

2.2 Oxidation, reduction and etherification of arabinoxylan

The overall aim of the chemical modifications studied in this work is to obtain improved melt processability and mechanical properties in the polysaccharide material. In general, a good material candidate would be processable by methods such as compression molding or extrusion, and exhibit ductility in mechanical testing. The chemical structure of the different derivatives is shown in Figure 2.2, with the carbon numbering of the carbohydrate rings and of some derivative functional groups.

Periodate oxidation

First reported by Louis Malaprade in 1926 [28], periodate oxidation using a periodate salt, such as sodium metaperiodate ($NaIO_4$), allows for selective cleaving of the C2-C3 bond in AX and other (β-(1→4) polysaccharides (Figure 2.2a-b). The reaction proceeds via a cyclic periodate ester intermediate which decomposes to give a dialdehyde group as the final product [29–31]. In AX, the viccinal diol on C2-C3 is the main functional group that can be oxidized by this reaction mechanism, barring side reactions involving radicals [32]. To reduce the extent of the side reactions, periodate oxidation is performed away from light, and with addition radical scavenger such as isopropanol [32]. In this thesis, periodate oxidized AX containing dialdehyde groups are referred to as dialdehyde AX (DAX).

Borohydride reduction

Dialdehyde derivatives of celluose, xylan, and by extension AX, are reported to exist as a mixture of free aldehyde, hydrated aldehyde, intra-chain and inter-chain hemialdal, and hemiacetal functionalities [33–35], shown in red in the second structure in Figure 2.2b. For oxidized xylan, there only minor presence of free aldehyde groups was reported [34]. In the presence of water and heat, the various aldehyde-derived functionalities can be converted back to free aldehyde groups [36]. To avoid cross-linking of polysaccharide chains in dialdehyde derivatives, a reduction with sodium borohydride ($NaBH_4$) into more chemically stable dialcohol groups [8, 32, 37], or further derivatization can be performed [38–40]. The reduction route with $NaBH_4$ to produce dialcohol AX (DiolAX) is studied in this thesis (Figure 2.2b).

Together, periodate oxidation and borohydride reduction results in a stable ring-opened derivative of polysaccharides [8, 32, 37]. These derivatives are of interest to the research community because it has been shown that ring-opening of the rigid polysaccharides results in an increase of the chain flexibility [41–43], which can lead to a lowering of the glass transition temperature (T_g). For example, through size exclusion chromatography with multi-angle light scattering (SEC-MALS), the Flory exponent was shown to decrease for dialdehyde cellulose [44], and the persistence length to decrease for oxidized alginate [45] and chitosan [46], all of which indicate lower stiffness in the oxidized chains after modification. Thermo-mechanically, dialcohol celluloses are more ductile [37, 47], have lower T_g than their unmodified counterparts [43], and can be thermally processed with water as a plasticizing agent [48]. A lowered T_g with oxidation has also been observed in dialdehyde xylan by dynamic mechanical analysis [42]. On the contrary, previous work on DAX showed neither a decrease in persistence length in SEC-MALS, nor a lowering of T_g in DMA [42].

Etherification with butyl glycidyl ether

Nucleophilic substitution with a butyl glycidyl ether (BGE) was used as the main etherification reaction in this thesis. It has been shown that further derivatization of DiolAX with BGE (Figure 2.2d) resulted in a material with T_g below 0 °C, that can be processed by compression molding, and exhibits film stretchability above 100% [49–51]. The combination of oxidation-reduction and etherification resulted in improved material ductility and melt processability compared to the etherification only process. At a degree of oxidation (DO) of 20 % BGE-DiolAX exhibited three to five times higher ductility compared to un-oxidized BGE-AX [8]. DiolAX etherified with BGE is referred to as BGE-DiolAX in this work. Any control samples with only substitution of BGE onto AX (skipping any ring-opening steps) will be referred to as BGE-AX.

Grafting of side chains to polysaccharide based materials has been performed before, in cellulose [52], chitosan [53], glucomannan [54] and xylan [11], for example. Fundador et al. [11] studied esterified xylans at the maximum theoretical degree of substitution (2 mol side chain per xylose unit), but did not test their melt-processability or their relaxation behavior by dynamic

mechanical analysis (DMA). The solvent casted films were stretchable up to 40% strain, but not to the same extent as the BGE-diolAX films [50]. The glucomannan esters studied by Enomoto-Rogers et al. [54] could act as an interesting comparison with BGE-DiolAX. The esterified glucomannans had high molecular weight (M_{w}), could be compression molded, and had good film ductility above 100% strain. The degree of substitution used were between 1.5 and 2.0.

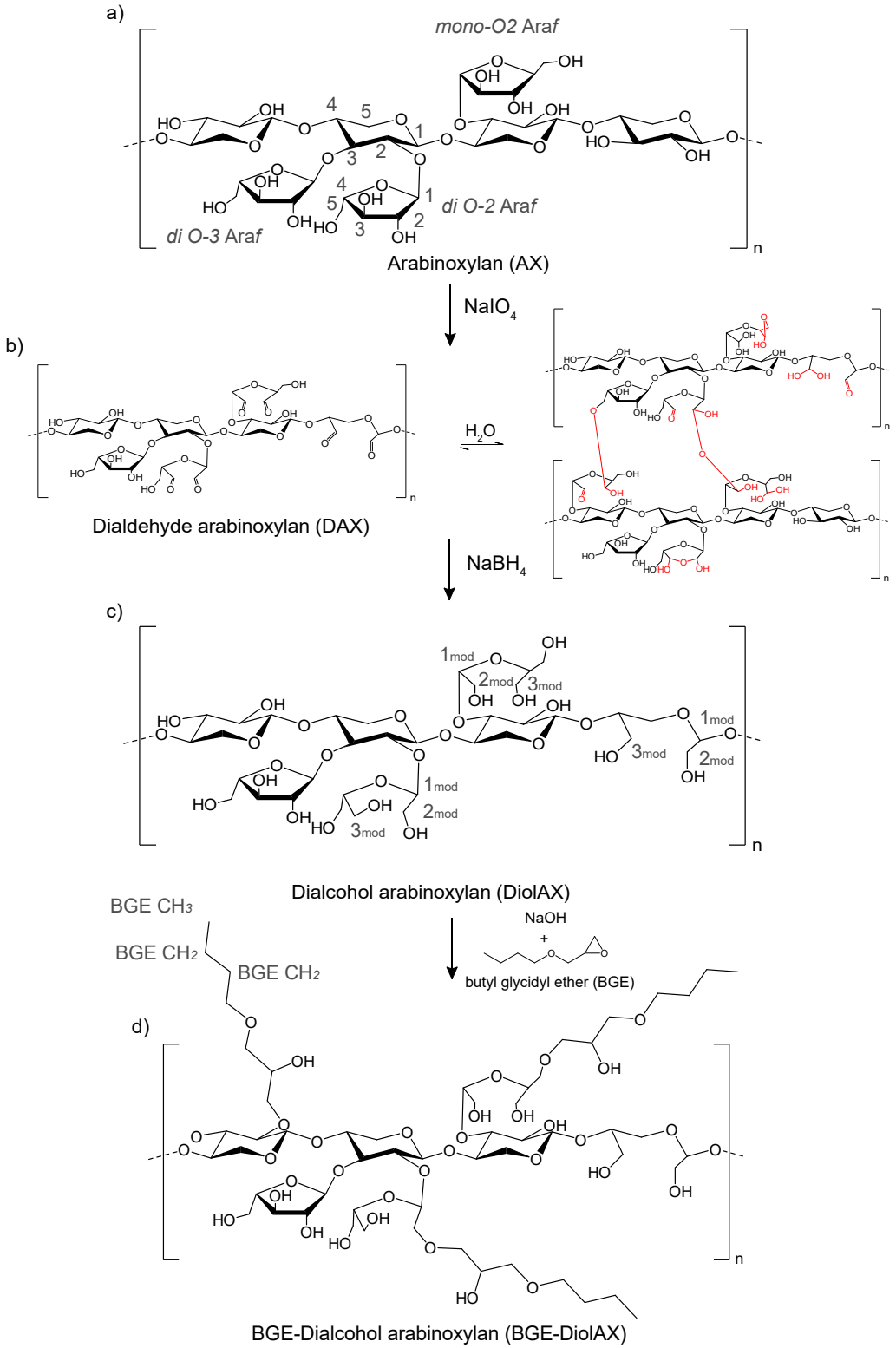

Figure 2.2: Schematic representation of the chemical structure of AX, dialdehyde AX, and dialcohol AX. Numbering of the carbons of the carbohydrate ring and of parts of the BGE side chain are also shown.

2.3 Structures of arabinoxylan materials

Figure 2.3 shows the approximate lengthscales of the structures investigated in this thesis, as well as the methods used to probe them. The structures of AX materials have been investigated in both solution/dispersion and solid-state. Solution in this work referring to AX chains dispersed as individual chains in solvent. When aggregation occurs the term dispersion is used instead. Those observed in solution are shown at the top of Figure 2.3, those observable in both states, such as the bond lengths, are in the middle, lastly, those observed in the solid-state are shown at the bottom of the figure.

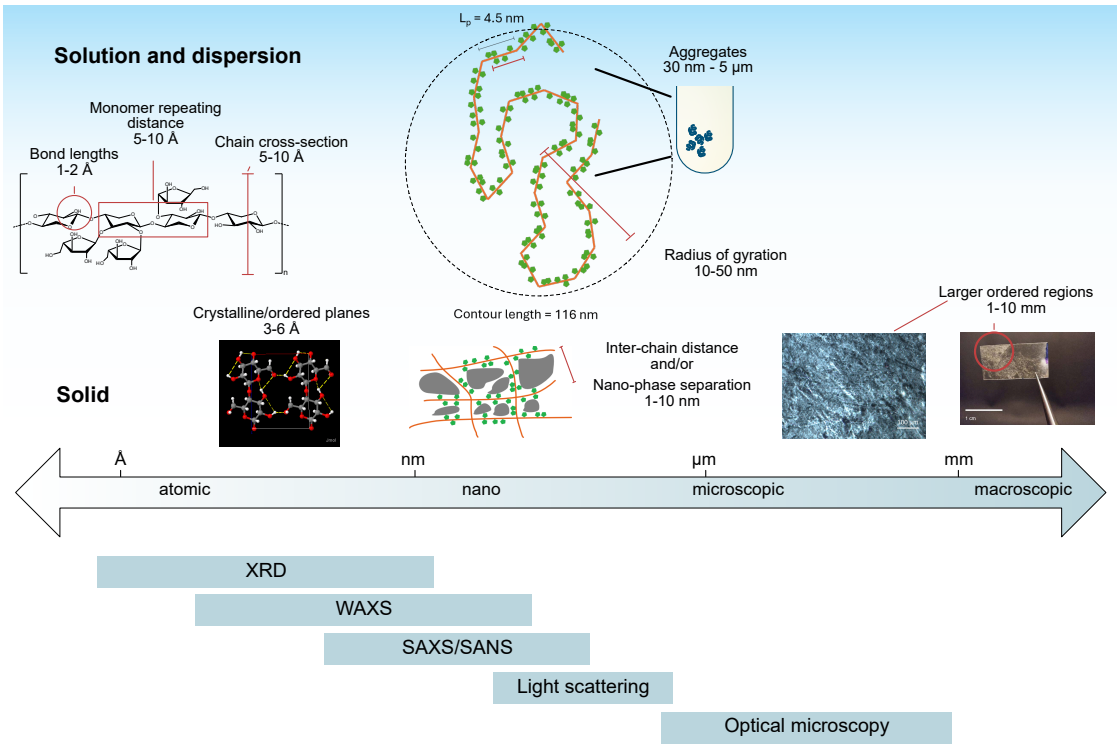

Figure 2.3: Schematic representation of the lengthscale of structures investigated in this thesis, as well as the methods used to probe them. X-ray diffraction (XRD), wide-angle X-ray scattering (WAXS), small-angle X-ray scattering (SAXS), persistence length (L_p). *The image of the cellulose crystalline plane has been used to represent possible ordered structures exhibited by polysaccharides: "Cellulose II AC plane", licensed under CC BY-SA 4.0. Source: Wikimedia Commons.*

Structures in solution and dispersion

The first hypothesis relates to evaluating the changes to the chain flexibility of AX. The investigation of said hypothesis involves measurement of the chain conformation of AX in solution or, in cases of incomplete solubility, in dispersion before and after chemical modification. We study as well, the changes in the

inter-molecular interactions of the materials by measuring the conformation at different concentrations.

A polymer's conformation in solution is described by its chain persistence length (L_p), the chain length or radius of gyration (R_g), and the chains' conformation statistics, often described with the Flory exponent (ν). For water-soluble AX, the chain conformation is typically described in literature as a semi-flexible chain [21, 23, 25, 55]. However, the exact rigidity of the AX chain has been an area where different values have been presented. A range of L_p values have been reported for AX, from 2 nm to 8 nm [21–24]. Earlier results have been based on measurements by SEC-MALS, where the L_p can be obtained through different approaches. The analysis is nontrivial and the obtained L_p vary depending on choice of model [24]. For example, Dervilly-Pinel, Thibault and Saulnier [23] calculated with a geometric formulae, obtaining values of 6 nm to 8 nm for the L_p of wheat flour. With the same dataset, Picout and Ross-Murphy [24] [24] obtained values of 3 nm to 5 nm for the L_p using the Burchard–Stockmayer–Fixman method. Also for wheat flour AX, Pitkänen et al. [22] reported L_p values close to 2 nm using the Bohdanecký model. While some variations in the results for L_p is expected, an AX chain with L_p of 2 nm, thus number of Kuhn segments per chain quite certainly greater than 10, can essentially be considered a Gaussian chain [24]. L_p values of 5 nm to 8 nm would describe AX as a semi-flexible polysaccharide similar to, for example, xyloglucan ($\sim$ 8 nm) [56].

Small-angle scattering experiments, with neutrons (SANS) or with X-rays (SAXS) can be used to probe the L_p more directly. The L_p is correlated to the crossover of the momentum transfer (q) between the regime in the high q region where the scattering intensity has a decay of $\sim q^{-1}$ (1D object), and the regime in intermediate q region where the scattering is driven by the solvent interactions which follows a $q^{-1.67 \text{ to } -3}$ scaling [57–59]. The transition between the two regions can be analyzed by a model-independent approach [57], or by fitting with polymer chain models [60] (Figure 2.4) to obtain a value for the L_p. Petermann et al. [25] obtained a fitting of wheat flour AX to a worm-like chain model with an L_p of 4.5 nm. Similar values were obtained from SAXS and SANS study of AX from *Plantago ovata* seed [61].

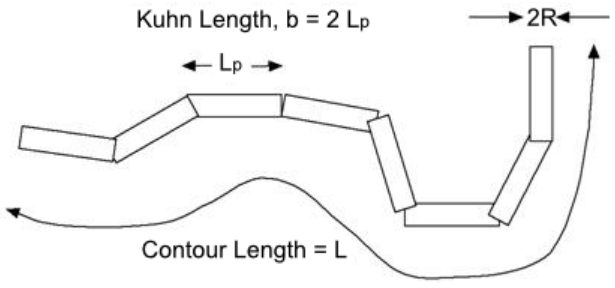

Figure 2.4: A description of a flexible cylinder chain model, showing the chain length, L_p and the chain cross-section radius (R). *Modified (for consistent symbol nomenclature) from the SasView documentation, https://www.sasview.org/docs/user/models/flexible_cylinder. Licensed under the BSD Three-Clause License.*

While the studies with SAXS/SANS have helped shed light on the conformation of AX in solution, some challenges and knowledge gaps remain. One, a systematic study across different A/X ratios has not been performed. It is possible, as discussed in section 2.1, that variation of A/X ratio and subsitution patterns may affect the conformation. Two, AX, like other polysaccharides [56] have tendencies to aggregate in solution. And the complete form factor can be obscured by contributions from the aggregates [25]. Lastly, to be certain that the form factor is probed, the fitting should be done for samples in the dilute regime. It would also be ideal if the structure factor, describing changes when chains interact at higher concentrations, is also described. Structure factors that can be used to model polymer chains in good solvents have been developed by Pedersen and Schurtenberger [62], from which one can assess the solvent quality by fitting the polymer's second virial coefficient (A_2) [62]. This allows assessment on whether modifications result in a change of the AX intermolecular interactions.

Structures in the solid-state

When studying atomic structures of AX (and other polysaccharide materials) in the solid-state such as by X-ray diffraction (XRD), one first observes the correlation length between covalent bonds at the highest q, around 3 $Å^{-1}$ or 2θ of 40° with wavelength λ of 1.54 Å (real space distance around 2 Å) [63]. This is then followed by a second peak representing interchain correlations, associated with larger distances ($\sim$ 5 Å), thus lower q, at around 1.4 $Å^{-1}$ ($2\theta = 20°$). For xylan, or low A/X ratio AX, ordered regions can occur (Figure 2.5), giving crystalline peaks that can be attributed to a repeating unit cell [27, 64–68]. For both xylan and AX, the structure was a left-handed threefold screw helix structure with two chains per unit cell stabilized by water [64, 68]. Highly substituted AX is mostly amorphous [27] while AX with substitution degrees below 0.3 are semi-crystalline, with assigned degrees of crystallinity between 10 - 20 % [27, 69].

When longer side groups are present in polymers such as through grafting of alkyl chains of length 5 to 10 carbons [70], an additional peak is observed in the 0.1 to 0.6 $Å^{-1}$ region. An example is shown from a study on poly(n-alkyl methacrylates) (PnMMA) (Figure 2.6), with the chemical structure in Figure 2.6b [70, 71]. The correlation peak occurs due to immiscibility between the side chains and the backbone leading to nanoscale separation (1 to 5 nm) (d_{II} in Figure 2.6c). The structure described is shown in Figure 2.6c. Lastly, a power law slope is typically observed at the lowest q in XRD, which is reflective of defects, pores or larger scale phase separation in the solid material [72].

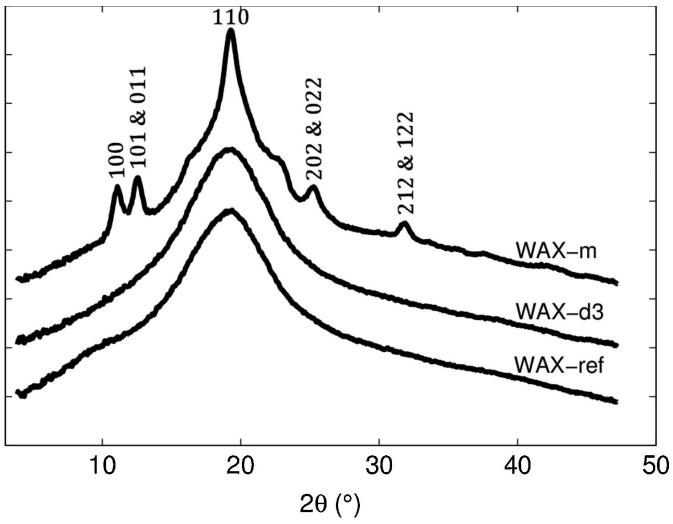

Figure 2.5: XRD data of AX with varying degrees of arabinose debranching (bottom to top) correlated with increasing intensity of crystalline peaks. With $\lambda = 1.54$ Å, 2θ conversion to q is as follows: $10° = 0.7$ Å^{-1}, $20°$ =1.4 Å^{-1}, $30° = 2.1$ Å^{-1}. Figure reproduced with permission from Heikkinen, S. L. et al., *Carbohydrate Polymers*, 2013. Copyright 2025 Elsevier.

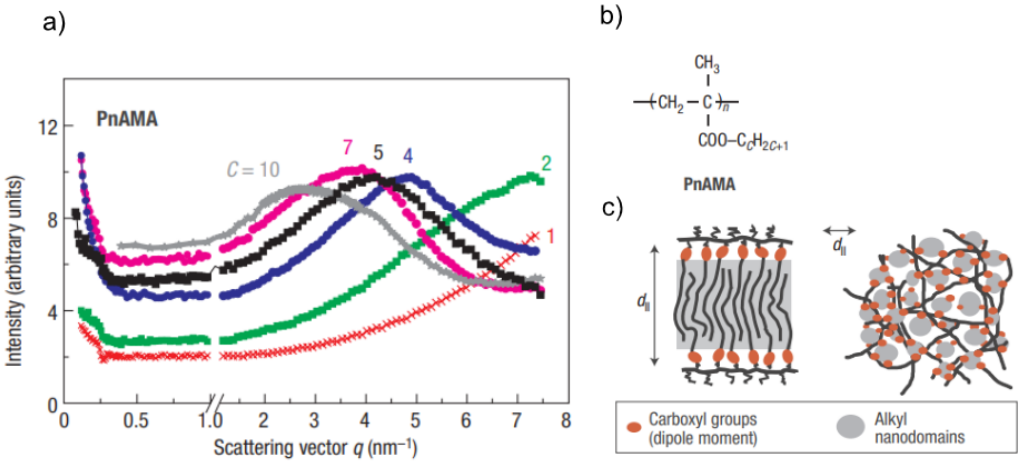

Figure 2.6: a) X-ray scattering data for different poly(n-alkyl methacrylates) (PnMMA), the number of carbon atoms in the alkyl side chain is indicated in the figure, b) chemical structure of (PnMMA), c) illustration of nanoscale phase separation in the system according to Beiner and Huth [70]. Figure reproduced from Beiner, M.; Huth, H., *Nature materials*, 2003 with permission from Springer Nature.

2.4 Dynamics of arabinoxylan materials

Dynamics observed by dynamic mechanical analysis

Dynamic mechanical analysis (DMA) measures the viscoelastic properties of materials, providing information on the dynamics of the system on the ms to second timescale. Although the accessible timescale can be expanded by a few orders of magnitude through superposition of data at different temperatures. A DMA measurement of a polymer involves imposing a sinusoidal force, typically strain, to the measured sample (within elastic deformation limits), and measuring the amplitude and phase shift of the response, here as measured stress. The response of an ideal elastic material, such as a metal, is in phase with the applied strain, while that of an ideal viscous material, such as water, is 90°out of phase.

A polymer/polysaccharide is a viscoelastic material, with the elastic component of the behavior described by the storage modulus and the viscous component by the loss modulus. In a temperature sweep experiment, changes in the storage and loss moduli provides information on the thermal relaxations occurring in the material, as in the example shown in Figure 2.7 for a polyester material [73]. For this material, the glass transition is the denoted as β, and the sub-glass transition as γ. The glass transition is marked by a sharp drop in the storage modulus (here G'), or a peak in the loss modulus (here G'').

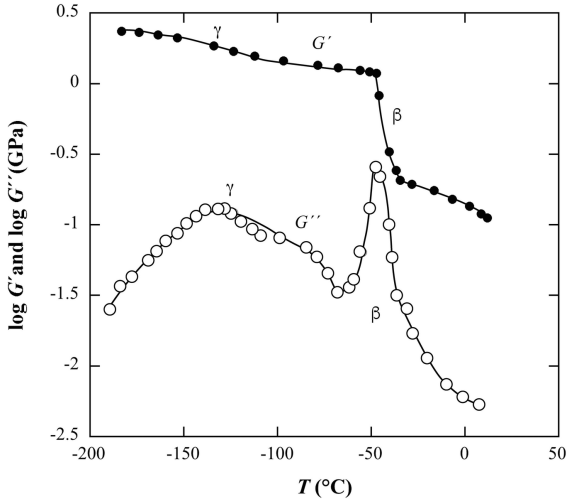

Figure 2.7: Shear storage G' and loss moduli G'' as a function of temperature for a polyester. Figure reproduced with permission from Gedde, U. W. et al., 2021. Copyright 2025 Springer Nature.

Dynamics observed by solid-state NMR

Dynamics with faster correlation times can be studied with NMR, in several cases, solid-state NMR can link the bulk properties of materials to their properties at the molecular scale [74]. A summary of the NMR methods and the correlation time they probe is shown in Figure 2.8 [74]. In this thesis, I

have focused on measurement of the proton relaxation time in the rotating frame ($T_{1\rho H}$) and of the dipolar lineshape, both of which probe dynamics at the kHz (10^{-4} s) scale. The kHz timescale should be sensitive to segmental motions of the chains in the AX materials. These have been chosen over the relaxation rates T_1 and T_2, which are more likely to be influenced by bond rotations [74, 75], although T_1 and T_2 measurements could be considered in the future as they provide complementary information on fast motions.

For the other techniques not studied in this work, ^{2}H relies on deuterium labeled polymers but has the advantage in that ^{2}H relaxation is affected by fewer parameters [74]. 2D exchange NMR is sensitive to changes in conformation (e.g. trans to gauche transitions) and other slower processes such as crystalline to amorphous exchange [74]. Chemical shift anisotropy (CSA) measures similarly slow changes in conformation, and relies on motions changing the orientation of polymer conformation relative to the magnetic field resulting in changes to the measured lineshape [74].

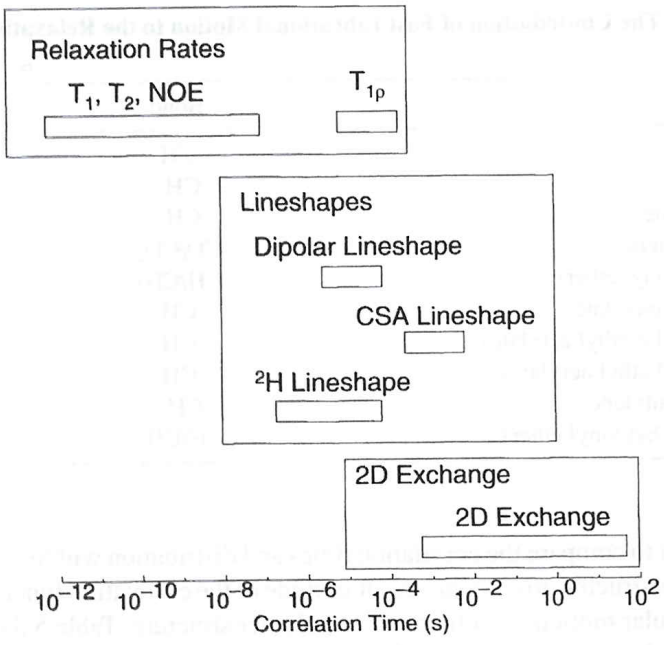

Figure 2.8: Schematic showing different correlation times probed by different solid-state NMR techniques. Figure reproduced with permission from Mirau, P. A., 2004. Copyright 2025 Springer Nature.

$T_{1\rho H}$ from CP/MAS NMR

Cross polarization (CP) is used to transfer magnetization from an abundant nuclei to a less abundant nuclei. In this thesis, the nuclei probed are ^{1}H and ^{13}C, respectively. CP was developed to enhance the signal of low abundance and low sensitivity nuclei such as ^{13}C [76, 77]. The transfer of magnetization occurs via heteronuclear dipolar interactions, which are affected by the mobility and proton environment of the nuclei [74]. The intensity of the magnetization at CP time (t) is given by

$$M(t) = \frac{M_{\text{eq}}\left[1 - e^{-\left(1+\frac{T_{\text{CH}}}{T_{1\rho\text{H}}}-\frac{T_{\text{CH}}}{T_{1\rho\text{C}}}\right)\frac{t}{T_{\text{CH}}}}\right] e^{-\frac{t}{T_{1\rho\text{H}}}}}{1+\frac{T_{\text{CH}}}{T_{1\rho\text{H}}}-\frac{T_{\text{CH}}}{T_{1\rho\text{C}}}} \tag{2.1}$$

With the general assumptions $T_{1\rho\text{H}} >> T_{\text{CH}}$ and the carbon relaxation time $T_{1\rho\text{C}} >> T_{\text{CH}}$, the intensity at contact time t can be simplified to

$$M(t) = M_{\text{eq}}(1 - e^{-t/T_{\text{CH}}})e^{-t/T_{1\rho\text{H}}} \tag{2.2}$$

where $M(t)$ is the measured intensity at CP contact time t, and the equilibrium intensity is M_{eq} (or M_0) [78]. The intensity increases as a result of polarization transfer from the protons to the carbons, with the transfer efficiency represented by the CP time constant T_{CH}, while the decay in intensity occurs as a result of $T_{1\rho\text{H}}$ relaxation [78].

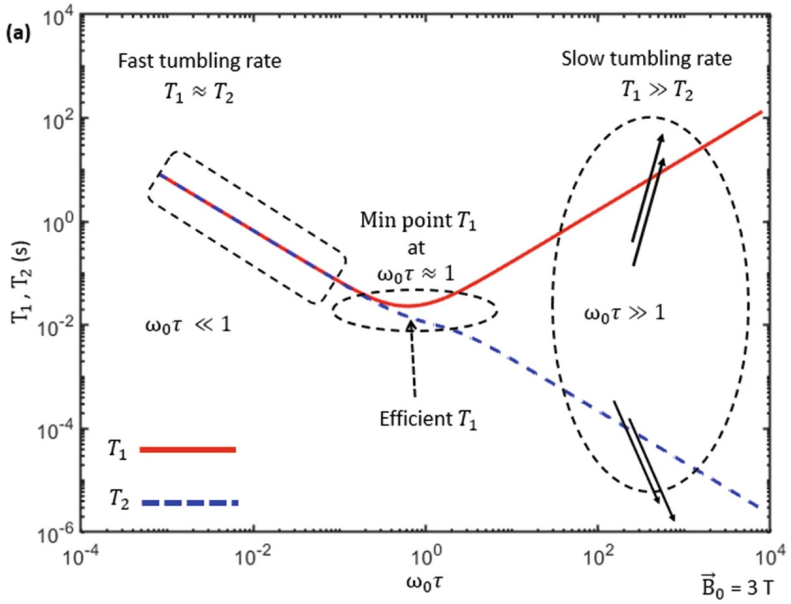

Figure 2.9: Dependence of T_1 and T_2 on the correlation time τ. Figure reproduced with permission from Khashami, F., 2024. Copyright 2025 Springer Nature.

In analyzing $T_{1\rho\text{H}}$, it is important to note that similar to T_1, $T_{1\rho\text{H}}$ has a hyperbolic shape with a minima at a certain correlation time τ (Figure 2.9). For T_1, the minima occurs at $\omega_0\tau = 0.6$, and for $T_{1\rho\text{H}}$ at $\omega_1\tau = 0.5$ [80], where ω_0 is the nuclei resonance frequency, and ω_1 is the product of the gyromagnetic ratio γ and the radiofrequency field B_1, giving $\omega_1 = \gamma B_1$ [80, 81]. When measured by CP/MAS, the minima for $T_{1\rho\text{H}}$ is in the range of the inverse of the spin-lock frequency [74]. We can gain knowledge of whether the molecular dynamics fall into the slow or fast regime by measuring at two temperatures or here, at two moisture contents, where water acts as a plasticizer for the AX materials. An increase or decrease in $T_{1\rho\text{H}}$ can then be correlated to changes in dynamics after modification of the AX material. Another important point is that $T_{1\rho\text{H}}$ is affected by spin diffusion, hence the nuclei in the same chain

segment may not have their relaxation times differentiated, and an average mobility of the chain is probed instead [74].

Proton dipolar linewidth from 2D NMR

The proton dipolar linewidth provides information on the extent of large-amplitude motions faster than dipolar coupling (50 kHz) which is correlated to a reduction of the proton dipolar line width [82]. A 2D heteronuclear version of the proton experiment was developed by Schmidt-Rohr, Clauss and Spiess [82] where a proton wideline spectrum is obtained for every ^{13}C resonance. The NMR experiment is called the Wideline-Separation (WISE) experiment [82].

The original WISE experiment by Schmidt-Rohr, Clauss and Spiess [82] was used to study a block copolymer of a 'rigid' polymer (polystyrene - PS) and a 'mobile' polymer (polydimethylsiloxane - PDMS). The WISE experiment can be performed with just the proton linewidth detection, followed by CP to ^{13}C, or with an additional mixing time (t_{m}) before CP that allows for spin diffusion of the protons. Using the first version, the narrow proton linewidth of the mobile PDMS and a broad linewidth of the PS can be clearly observed as in Figure 2.10a. With the second version, spin diffusion results in the mixing of the proton magnetization (and of the t_1 modulation), thus the rigid region shows components of the mobile region, and vice-versa (Figure 2.10b-c). What one obtains from the second version of the experiment is an estimation of the distance of the spatial separation between the rigid and mobile components based on the evolution of the linewidth with mixing time [82].

Radloff, Boeffel and Spiess [83] later used the WISE experiment to study the water environment around cellulose. At $t_{\mathrm{m}} = 0$ ms, only broad peaks from the rigid cellulose chains are observed. Then, at $t_{\mathrm{m}} = 5$ ms, mobile contributions from water protons begin to appear due to spin diffusion. From their WISE experiments, the authors estimated the water-cellulose distance as 1 nm or below. In this thesis, the WISE experiment was used with the interpretation that when $t_{\mathrm{m}} \approx 0$ ms, the individual proton linewidth of each carbon nuclei in AX should be observable, which would allow observation of an increase in mobility at a specific site from the modification reactions.

Dynamics observed by quasielastic neutron scattering

Quasielastic neutron scattering (QENS) is another characterization method that is sensitive to the dynamics of materials, but on the shorter timescale, typically on the order of picoseconds to nanoseconds. QENS is also a (neutron) scattering method, sharing similarities with SAXS and SANS, where momentum transfer between the incident wavevector (k_{i}) and final scattered wavevector (k_{f}) are measured. The scattering function $S(q, \omega)$ contains information on both the scattering vector q and energy transfer ω. In diffraction and small-angle scattering, it is the position of scattering objects that is of interest, and the assumption is made that all scattering events are elastic; the incident and final wavevectors do not change ($k_{\mathrm{i}} = k_{\mathrm{f}}$). In a QENS experiment, both the scattering vector and energy transfer is measured, allowing for the study of

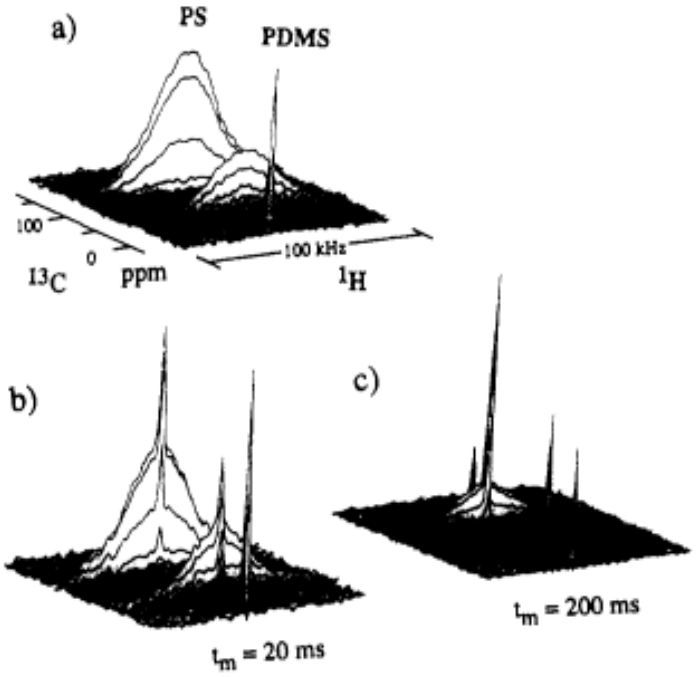

Figure 2.10: WISE-NMR spectra of PS-*b*-PDMS for a series of mixing times a) $t_\mathrm{m} = 0$ ms, b) $t_\mathrm{m} = 20$ ms, c) $t_\mathrm{m} = 200$ ms. Figure reproduced with permission from Schmidt-Rohr, K.; Clauss, J.; Spiess, H. W., *Macromolecules*, 1992. Copyright 2025 American Chemical Society.

the lengthscale (from q) and timescale (from ω) of dynamics occurring in the sample.

A QENS spectra from poly(hexylene oxide) (PHO) reproduced from Gerstl et al. [84] is shown in Figure 2.11. The region at zero energy transfer $\mathrm{S}(q, \omega = 0)$ is the elastic peak, where neutrons are scattered without energy exchange. The broad feature centered within approximately ± 1 meV is referred to as the quasielastic region, and arises from processes such as rotational or diffusive motions in the polymer [85]. Qualitatively, the decrease in the elastic peak at 310 K compared to 175 K indicates a clear increase in the mobility of the polymer system, as is expected when above the T_g of PHO (205 K) [84]. Compared to the instrumental resolution (black lines in Figure 2.11), the width of the quasielastic region at 175 K is relatively q independent, while relative contribution changes with q. This is indicative of localized motions. At 310 K, the width of the quasielastic region is strongly q dependent, indicating contributions from diffusive motions [84, 86].

In addition to measuring the full QENS spectra at a set temperature, it is also possible to perform a scan at only a fixed energy, e.g. $\omega = 0$ µeV, or $\omega = 3$ µeV. This is known as a fixed-window scan (FWS), and provides information similar to that offered by differential scanning calorimetry (DSC), with additional information in the q dimension. Especially in the case of inelastic FWS ($E \neq 0$), the q dependence allows for localized motions to be distinguished from diffusive motions as discussed for the full QENS spectra. An example of an elastic FWS is shown in Figure 2.12 from polypropylene [87].

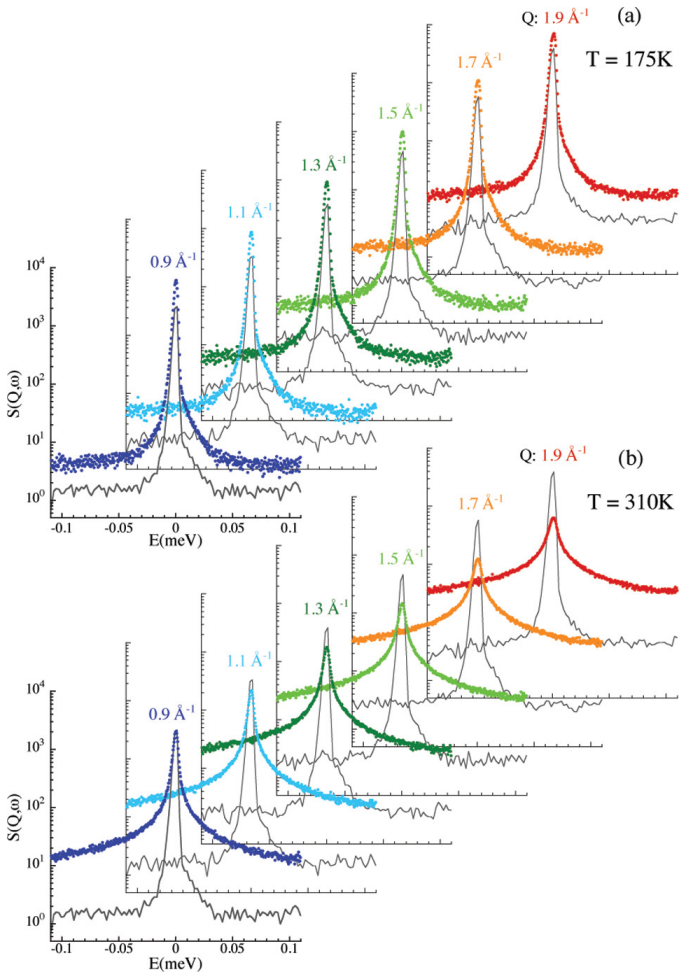

Figure 2.11: QENS data for polyhexylene oxide at different q values, a) in the glassy state (T = 175 K), and b) in melt (T = 310 K). Figure reproduced with permission from Gerstl, C. et al., *Macromolecules*, 2012. Copyright 2025 American Chemical Society.

The decrease in elastic intensity between 2K $< T <$ 100K is attributed to the Debye-Waller factor, then, at 100 K $< T <$ 266 K the motions of CH_3 bonds are observable. Finally, above the T_g at 266 K, a large decrease in the elastic intensity occurs due to the onset of segmental motions [87].

An example of an inelastic FWS with E = 1 µeV and 3 µeV is shown in Figure 2.13a, here of proton rotation in KB_4. The maxima of the inelastic FWS peaks is similar at the different q values, indicating the localized character of the motion. Another example from a mixture of glycerol/water is shown in Figure 2.13b, where the maxima of the inelastic FWS is q dependent as a result of the motions being diffusive in character [88].

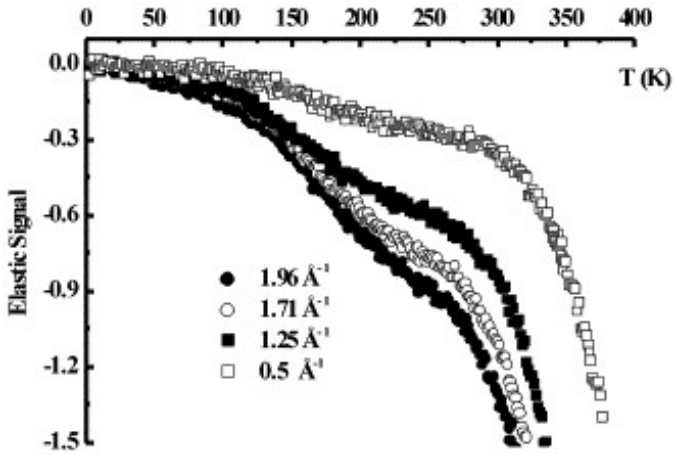

Figure 2.12: Elastic FWS of polypropylene at different q values. Figure reproduced with permission from Arrighi, V. et al., *Physica B: Condensed Matter*, 2001. Copyright 2025 Elsevier.

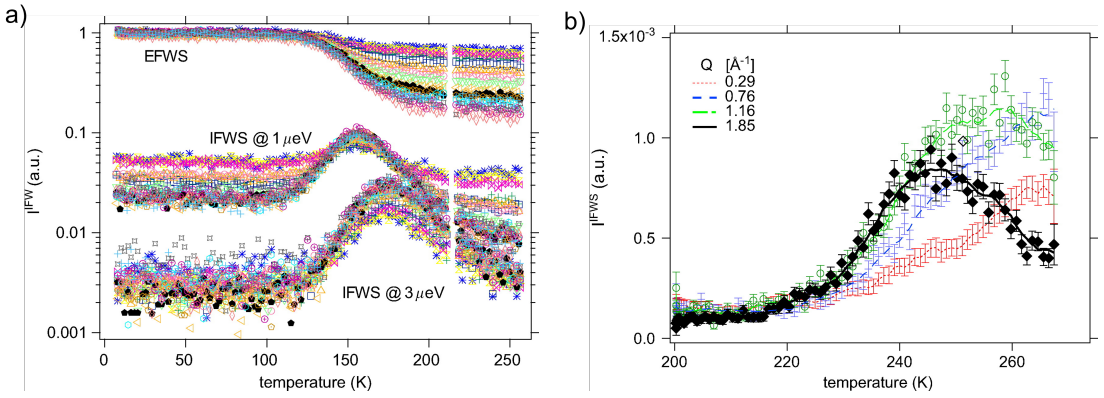

Figure 2.13: a) Elastic and inelastic FWS of KB_4, and b) of glycerol/water mixture at different q values. Figure reproduced with permission from Frick, B.; Combet, J.; van Eijck, L., *Nuclear Instruments and Methods in Physics Research Section A: Accelerators, Spectrometers, Detectors and Associated Equipment*, 2012. Copyright 2025 Elsevier.

Chapter 3

Materials and methods

3.1 Extraction of arabinoxylan

AX was isolated from wheat bran on a 1 kg scale through alkaline extraction, described in more detail in paper IV. Briefly, milled wheat bran was pretreated in acid, delignified with $NaClO_2$ and AX was extracted under alkaline conditions with $Na_2S_2O_4$ as a reducing agent. The hemicellulose-rich liquid fraction was separated from cellulose by centrifugation. The extracted hemicellulose dispersion containing AX was concentrated to half-volume and precipitated in increasing concentration of ethanol (20, 40, 60 and 80% v/v) in order to obtain AX fractions with different A/X ratios based on their water solubility. The precipitate was then recovered by centrifugation and dialyzed against DI water through a dialysis membrane with cutoff of 3.5 kDa. A summary of the different AX fractions used in this work, as well as further derivatization routes is shown in Figure 3.1. The AX fractions are named after their respective A/X ratios.

3.2 Chemical modification of arabinoxylan

The extracted AX with varying A/X ratios were subsequently modified by periodate oxidation, borohydride reduction and etherification.

Periodate oxidation

Details on the reaction conditions can be found in papers II, III and IV. In general an aqueous solution of AX at a concentration of 20 $mg \cdot mL^{-1}$ was heated until dissolution of AX was achieved. Then, isopropanol was added as a radical scavenger [32] followed by an amount of $NaIO_4$ corresponding to the desired degree of oxidation (between 0.25 and 0.50 mol equiv.) The reaction flask was covered with aluminium foil to protect from light and stirred at room temperature until no further changes were observed in the $NaIO_4$ concentration measured using UV-vis spectroscopy. The reaction mixture with DAX was

used as is for the next reaction step, or isolated by dialysis and subsequent freeze drying.

Borohydride reduction

$NaBH_4$ and NaH_2PO_4 was dissolved in DI water, then added to the DAX dispersion. The reduction was performed with stirring for 4 h at room temperature. The samples were then purified through dialysis against DI water. The reaction mixture containing DiolAX was used for the next reaction step, or freeze dried to obtain DiolAX.

Etherification with butyl glycidyl ether

The DiolAX solution from the previous step was concentrated in a rotary evaporator, resulting in a concentration of ca. 4% DiolAX in water. The DiolAX dispersion was added to a three-necked round-bottom flask equipped with a reflux condenser and nitrogen inlet. Then, NaOH was added, stirred for 1 h, after which BGE was slowly added to the solution through a needle over 30 min. The mixture was stirred overnight at 45 °C. After the reaction, the solutions were neutralized with 1 M H_2SO_4 and dialyzed against DI water. The BGE-DiolAX was recovered by centrifugation and dried in a convection oven at 30 °C.

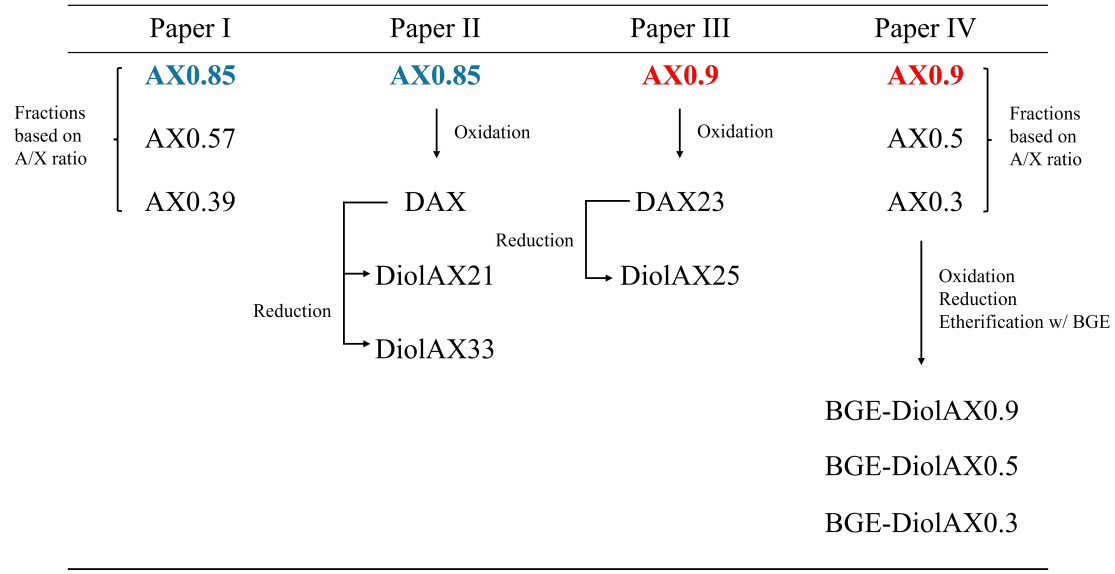

Figure 3.1: AX fractions used in this work, as well as the different derivatives produced from them. Colors indicate shared material fractions across the different papers/manuscripts.

3.3 X-ray scattering

In **paper I**, SAXS experiments were performed at the CoSAXS beamline at MAX IV laboratory. An X-ray wavelength (λ) of 1.0 Å was used, detection was

done simultaneously on the SAXS detector Eiger2 4M (Dectris AG, Switzerland) and the WAXS detector Pilatus3 2M (Dectris AG, Switzerland). The detectors were positioned at distances of 10.12 m (SAXS) and 0.57 m (WAXS) from the sample, covering a q range from 0.0013 $Å^{-1}$ to 0.94 $Å^{-1}$. Samples were injected into a flow capillary system with a BioSAXS autoloader. Data reduction is carried out using the python implementation of MatFRAIA [89] for radial integration. The integrated data are normalized to the X-ray beam transmittance and averaged, following data rejection using correlation maps to exclude any effects of radiation damage or inhomogeneities in the sample. Background subtraction and scaling to water absolute intensities were carried out using Python scripts in Jupyter Notebook.

Complimentary SAXS measurements were performed on a Xeuss 2.0 instrument (Xenocs, France). A Cu α source with λ of 1.54 Å was used, collection was done with an Pilatus3 detector (Dectris AG, Switzerland), and two sample to detector distances of 2490 mm, with a collimated beam size of 0.5 mm × 0.5 mm, and 340 mm, with a collimated beam size of 0.8 mm × 0.8 mm were used to cover a q range of 0.0045 $Å^{-1}$ to 1.8 $Å^{-1}$. The scattering signals from the empty beam, empty capillary, and dark field were measured separately, and subtracted.

In **paper II**, the same configuration as for paper I was used for isolated samples measured with the BioSAXS autoloader. For the time-resolved experiment, detectors were positioned at distances of 2.16 m (SAXS) and 0.57 m (WAXS), covering a q range from 0.0052 $Å^{-1}$ to 0.94 $Å^{-1}$. For the isolated samples, detector distances were 10.12 m (SAXS) and 0.57 m (WAXS), covering a q range from 0.0013 $Å^{-1}$ to 0.94 $Å^{-1}$. For the time-resolved experiment, averaging was performed manually with a Python script. Otherwise, data reduction, averaging, scaling and subtraction were performed as in paper I, with small modifications to the background subtraction script in Python.

In **paper IV**, SAXS and WAXS data were collected on a SAXSLAB Mat:Nordic (SAXSLAB, Denmark) benchtop instrument with a Cu Kα radiation source, covering a q range from 0.01 $Å^{-1}$ to 2.7 $Å^{-1}$. The detector distance was 477 mm and 126 mm for SAXS and WAXS, respectively. q-calibration was performed using silver behenate powder. Compression molded BGE-DiolAX films were sandwiched between two Kapton films and clamped to a solid sample holder, while the AX0.9 sample was solvent casted and measured as a self-standing film. The direct beam intensity was measured to determine the absolute intensity of the measured scattering patterns. Data reduction was done with the SAXSGUI software (version 2.27.03). Thickness correction and subtraction of the Kapton background were done using Matlab scripts.

3.4 Models describing the scattering of polymers in solution

Two polymer chain models were used to describe SAXS data of AX and derivatives in solution. The first is the flexible cylinder model which contains

terms describing the chain contour length, Kuhn length and the cross-section radius (R_{xs}) [60, 62]. The flexible cylinder model has been derived for chains in good solvent conditions (positive excluded volume), and that of chains in theta solvent conditions (zero excluded volume) [60], hence its limitations for chains in poor solvent conditions.

The second is the more general polymer with excluded volume model, which contains terms describing the R_{g}, and the exponent that can be interpreted as the inverse of the Flory exponent when applied to polymer conformational statistics [90]. This model is more general as it applies to polymer chains with exponent between 5/3 to 3. It does not, however, describe the Kuhn length, R_{xs} and does not provide a relation between R_{g} and the chain contour length. The version implemented in SasView was used (*https://www.sasview.org/docs/user/models/polymer_excl_volume*).

In paper I, the flexible cylinder model was modified to better account for different structural features at low q and high q. An additional power law structure factor was added to account for aggregate contributions at low q. A and n are fitting constants describing the power law background, and the factor of 0.01 was added for numerical stability reasons. At high q, to account for molecular scattering from the arabinose or xylose units at high q [91, 92], a Gaussian chain function [93], with radius of gyration $R_{\mathrm{g,\ mol}}$ and scale factor B, was added. $\mathrm{P_{sc}}$ is the single chain form factor, given by the scattering functions of excluded volume chains, $P_{\mathrm{chain}}(q)$ and $P_{\mathrm{rod}}(q)$, with interpolation and correction factors $\chi(q, L, b)$ and $\Gamma(q, L, b)$ (Equation 3.3). $\mathrm{S_{xs}}$ is the cross section scattering function representing the flexible cylinder model, where R_{XS} is the cylinder cross section radius and $B_1(x)$ is the Bessel function of first kind and first order[62]. Lastly, bkg is the q-independent background.

$$I(q) = I_0 P_{\mathrm{sc}}(q) S_{\mathrm{xs}}(q) \left(1 + A\left(\frac{0.01}{q}\right)^n\right) + \frac{I_0}{B}\left(\frac{2\left[\exp(-Z) + Z - 1\right]}{Z^2} - P_{\mathrm{sc}}(q) S_{\mathrm{xs}}(q)\right) + bkg \quad (3.1)$$

$$Z = (qR_{\mathrm{g,\ mol}})^2 \quad (3.2)$$

$$P_{\mathrm{sc}}(q) = [P_{\mathrm{chain}}(q)(1 - \chi(q, L, b)) + P_{\mathrm{rod}}(q)\chi(q, L, b)]\Gamma(q, L, b) \quad (3.3)$$

$$S_{\mathrm{xs}}(q) = \left[\frac{2B_1(qR_{\mathrm{xs}})}{qR_{\mathrm{xs}}}\right]^2 \quad (3.4)$$

To describe the scaling of the scattering intensity with increasing concentration according to polymer scaling laws [62], we use the polymer reference interaction site model (PRISM) model described by Pedersen and Schurtenberger [62]. A rod form factor was used for the screening correlation function $c(q, L_{\mathrm{PRISM}})$ with rod length L_{PRISM}. The PRISM model scaling is applied

to the first and second terms describing the flexible cylinder and power law background in Equation 3.1, the remaining terms are unchanged. The $I(q)$ is then given as

$$I_{PRISM}(q) = \frac{I_0 P_{sc}(q) S_{xs}(q)}{1 + \beta c(q) P_{sc}(q)} \left(1 + A\left(\frac{0.01}{q}\right)^n\right) + \frac{I_0}{B}\left(\frac{2\left[\exp(-Z) + Z - 1\right]}{Z^2} - P_{sc}(q)S_{xs}(q)\right) + bkg \quad (3.5)$$

$$\beta = 2MA_2c \quad (3.6)$$

where A_2 is the second virial coefficient, M is the molar mass and c is the polymer concentration.

The second model; polymer chains with excluded volume (P_{exc}, was modified to include the power law structure factor describing the low q aggregate contributions. The other terms and the concentration dependent structure factor were not added. This model was used to describe AX dispersions which were in poor solvent conditions and did not display prominent features from R_{xs} or Kuhn length. The model then takes the form

$$I(q) = scale \cdot P_{\text{exc}}(q)\left(1 + A\left(\frac{1}{q}\right)^n\right) + bkg \quad (3.7)$$

3.5 NMR spectroscopy

In **papers I and II**, NMR measurements were performed on an Oxford 800 MHz magnet, with the Bruker Avance III HD spectrometer equipped with a 5 mm TXO cryoprobe at 45 °C. ^{13}C spectra were collected using the zgig sequence with 192 scans, and a D1 delay of 5 sec. Phasing and background subtraction was performed on Topspin 4.3.0.

In **paper III**, freeze dried samples were stored for over 48 hour either in a low humidity environment or at 53% relative humidity (RH). For the former, a glass jar filled with silica gel was used (< 20% RH), and for the latter a glass jar filled with saturated $Mg(NO_3)_2$ solution was used. Solid-state MAS experiments were performed in a 16.4 T magnetic field on the Bruker Avance III HD spectrometer equipped with a 4 mm HXY MAS probe operating in ^{1}H/^{13}C double-resonance mode at a MAS rate of 4 kHz. Carbon spectra (^{1}H-^{13}C CP) were acquired with 512 scans, a relaxation delay of 3 s and an acquisition time of 6 ms. The ^{1}H 90° pulse was 3.03 µs. The CP mixing time was between 25 µs and 10 ms and employed 80-100% ramp on the ^{1}H channel at 42 kHz rf field strength, and with rf field strength of 38 kHz on the ^{13}C channel. The SPINAL-64 program was used for ^{1}H decoupling during acquisition with a field strength of 100 kHz. Phasing and baseline correction was performed in Topspin 4.3.0. ^{13}C intensities were integrated and fitted to the model in Equation 2.2 to obtain the ^{1}H $T_{1\rho}$ and T_{CH} with a Python script.

2D ^{1}H-^{13}C HETCOR experiments were recorded with 64 scans, a 114 µs acquisition (32 points) in the indirect ^{1}H dimension and a 300 µs CP contact time with the same CP conditions as mentioned above. 2D ^{1}H-^{13}C WISE experiments were conducted with the same settings as the HETCOR with the ^{1}H spin diffusion period varied between 10 µs and 10 ms.

3.6 Quasielastic neutron scattering

Quasielastic neutron scattering (QENS) experiments were performed on three different instruments, each with a different energy resolution and energy transfer range. The instruments were OSIRIS at the ISIS neutron and muon source, and IN16b and SHARPER, at the Institute Laue Langevin (ILL). To reduce the contributions from H nuclei in water but still have the same conditions as in the NMR experiments, AX and DiolAX films were dried in a vacuum oven at 50 °C overnight, and equilibrated in a humidity jar with saturated $Mg(NO_3)_2$ in D_2O solution.

Measurements on OSIRIS were performed with the pyrolitic graphite (002) setup, giving an energy resolution of 25.4 µeV and energy transfer range $-0.57 \leq \omega \leq 0.69$ meV. Solvent casted films (for AX, DiolAX) or compression molded films (BGE-AX, BGE-DiolAX) with dimensions $l \times w \times t$ of 40×40×0.17 mm were placed in flat aluminum sample holders with thickness 0.2 mm or 0.3 mm and sealed with indium wire. The spectra of vanadium was used for the resolution function.

Measurements on IN16b, Si(111) monochromaters and analyzers were used, providing an incident neutron wavelength of 6.271 Å, energy resolution of 0.75 µeV, and energy transfer range $-0.031 \leq \omega \leq 0.031$ meV. Elastic (energy transfer $\omega \approx 0$) and inelastic ($\omega = 3$ µeV) fixed window scans (FWS) were measured as a function of temperature between 2 K and 360 K. The spectra of the sample at 2 K was used for the resolution function.

Measurements on SHARPER used an incident wavelength of 6 Å, giving an energy resolution of 55 µeV and energy transfer range of approximately $-5 \leq \omega \leq 1$ meV. The spectra of the sample at 2 K was used for the resolution function. On both ILL spectrometers, films of the sample were placed in aluminium foil satchels and rolled into cylindrical cans of diameter 15 mm. The cans were then sealed with lead wire.

Chapter 4

Results and discussion

An assessment of the evolution of AX structure with modification requires that a good understanding of their structure is known prior to modification. Another variable to take into consideration is that atomic and nano-scale structure of AX may vary with their A/X ratio and substitution patterns. AX fractions from wheat bran each with different A/X ratio were successfully obtained by solvent fractionation and were then studied to answer the proposed hypotheses.

The monosaccharide composition characterization by HPAEC were consistent across two different hydrolysis procedures, H_2SO_4 and trifluoroacetic acid (TFA), and were in agreement with those estimated from ^{13}C NMR. The compositions of the main fractions AX used in this work are shown in Table 4.1.

Table 4.1: Monosaccharide composition, galacturonic acid (GalA), glucuronic acid (GlcA), acid soluble lignin (ASL) and insolubles, as determined using H_2SO_4 and trifluoroacetic acid (TFA) hydrolysis procedures and characterized by HPAEC. The arabinose/xylose (A/X) ratio calculated ^{13}C NMR of non-hydrolyzed samples are also shown. Adapted from Janewithayapun, R. et al., *Carbohydrate Polymers*, 2025 under the CC-BY license. *n.d. means that this component was not detected. *Determined using retention time rather than MALS*

Component (wt%)	**AX0.39**		**AX0.57**		**AX0.85**		**AX0.9**
	H_2SO_4	TFA	H_2SO_4	TFA	H_2SO_4	TFA	H_2SO_4
Arabinose	28	26	29	33	42	43	41
Rhamnose	n.d.	n.d.	n.d.	n.d.	n.d.	n.d.	n.d.
Galactose	n.d.	2	3	4	4	4	3
Glucose	n.d.	3	8	6	n.d.	1	3
Xylose	62	67	53	56	46	50	44
Mannose	n.d.	n.d.	n.d.	n.d.	n.d.	n.d.	n.d.
Insolubles	6	-	4	-	5	-	5
ASL	3	-	3	-	4	-	4
GalA	-	0	-	1	-	1	-
GlcA	-	2	-	1	-	1	-
A/X ratio	0.45	0.39	0.55	0.58	0.90	0.86	0.93
A/X ratio from ^{13}C NMR	0.34		0.57		0.80		-
M_w from DMSO SEC-MALS	120 kg · mol^{-1}		170 kg · mol^{-1}		220 kg · mol^{-1}		*330 kg · mol^{-1}

4.1 Chain conformation of arabinoxylan in water dispersion

Conformation of arabinoxylan under dilute conditions

SAXS data of AX0.39, AX0.57 and AX0.85 water dispersions at concentrations representing dilute conditions (1 and 4 mg·mL^{-1}) are presented in Figure 4.1, with fits to models described below. The scattering profile of the AX dispersions at 1 mg·mL^{-1} indicate dispersed AX chains, with minor contributions from larger aggregates for all three A/X ratios.

At the highest q values, we observe scattering from the AX chains' cross-section [56], then, at around $q = 0.2$ Å^{-1} there is a cross-over to a $\sim q^{-1}$ scaling characteristic of scattering from a rod-like object [56, 57]. The length of the q^{-1} region (towards lower q) is indicative of different the L_p in the three AX materials. Through fitting of the flexible cylinder model described in Equation 3.1 and Figure 2.4, the L_p of AX0.85 was obtained as 4.5 nm. AX0.57 and AX0.39 could not be fitted with a polymer model that has L_p parameters, as these models have been developed for chains in theta or good solvent conditions [60], while AX0.57 and AX0.39 behave as compact chains under poor solvent conditions, described in more detail below. The L_p was therefore, estimated roughly from the transition point of the q^{-1} scaling to intermediate q region scaling. The relation is then $L_p = 6/\pi q$ [57, 95], giving L_p values of 3.8 nm for AX0.57 and 1.5 nm for AX0.39.

In the intermediate q region between $0.009 < q < 0.06$ Å^{-1} for AX0.85 and AX0.57, and $0.009 < q < 0.1$ Å^{-1} for AX0.39, the AX conformation statistics are probed. The exponent of the q decay in this region represents ($q^{-1/\upsilon}$), where ν is the Flory exponent describing the interactions between AX chain and the solvent [56, 59]. AX0.85 has a scattering intensity that scales with $q^{-1.7}$ ($\nu \approx 0.59$) - indicating that AX0.85 behaves as an extended chain in a good solvent environment. The AX0.57 and AX0.39 have a scaling of $q^{-2.3\ to\ -2.5}$ from fitting to Equation 3.7, which is indicative of a more compact structure, and therefore, poor AX-water interactions in comparison to AX0.85.

At lower q values ($q < 0.009$ Å^{-1}) the scattering intensity begins to level out into the Guinier region, where the radius of gyration (R_g) of a chain is probed. In this q-range, we also observe contributions from larger aggregates in all samples ($q < 0.003$ Å^{-1}).

AX with higher A/X ratios adopt more extended conformations in water dispersions. Variations were observed in both the L_p, and the statistical conformation of the chains. Higher degree of substitutions of arabinose on the xylose backbone have been discussed to reduce inter-molecular interactions in AX [20, 21], thereby allowing AX to interact more favorably with the solvent. This explanation is in agreement with SAXS results obtained in this study.

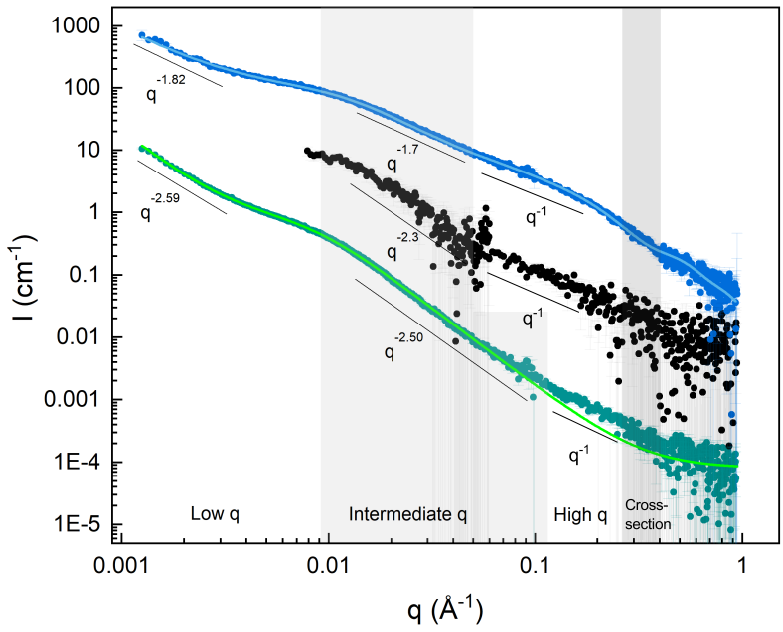

Figure 4.1: SAXS data from dispersions at 1 mg·mL^{-1} in water for AX0.39 (green), AX0.57 (black), AX0.85 (blue). Data scaled by factors of 1, 50, and 1000 for AX0.39, AX0.57, AX0.85 respectively for readability. Lines for AX0.85 and AX0.39 show fit to the models described. Adapted from Janewithayapun, R. et al., *Carbohydrate Polymers*, 2025 under the CC-BY license.

Structure factor and the solvent interactions of arabinoxylan

The scattering intensity of AX0.85 as a function of concentration shows scaling behavior similar to those of polymer solutions in a good solvent [96]. This occurs as the polymer chains begin to entangle and interact at concentrations in the semi-dilute regime. In this regime, the polymer chain is not fully extended and forms regions of correlation blobs, leading to a low q scattering intensity that decreases relative to concentration (Figure 4.2a) [96]. Following the approach of Pedersen and Schurtenberger [62], we added the polymer reference interaction site model (PRISM) as a structure factor (Equation 3.5), allowing us to describe the scattering intensity of AX0.85 over the different concentrations.

The Kuhn length and contour length were fixed to the value obtained at the most dilute concentration of 0.25 mg·mL^{-1}, and the other parameters were fitted ($I(0)$, R_{xs}, aggregate parameters, molecular scattering parameters and β). The model follows the trend of the concentration dependent behavior well (Figure 4.2a). The fitted β was plotted against the true relative concentration, which was obtained from normalization of each concentration to the same high q intensity (Figure 4.2b). From the slope of the plot $= 2MA_2c$, we obtain $A_2 = 54.4M$ (with c in units of g $\cdot$ mL^{-1}). Using $M = 220000$ g·mol^{-1} obtained from SEC-MALS of AX0.85, we obtain $A_2 = 0.00025$ mol·mL·g^{-2}. The obtained positive A_2 is expected from a polymer chain in good solvent conditions [97].

Both AX0.57 and AX0.39 did not disperse as well as AX0.85 did, instead showing trends towards forming larger structures at higher concentrations,

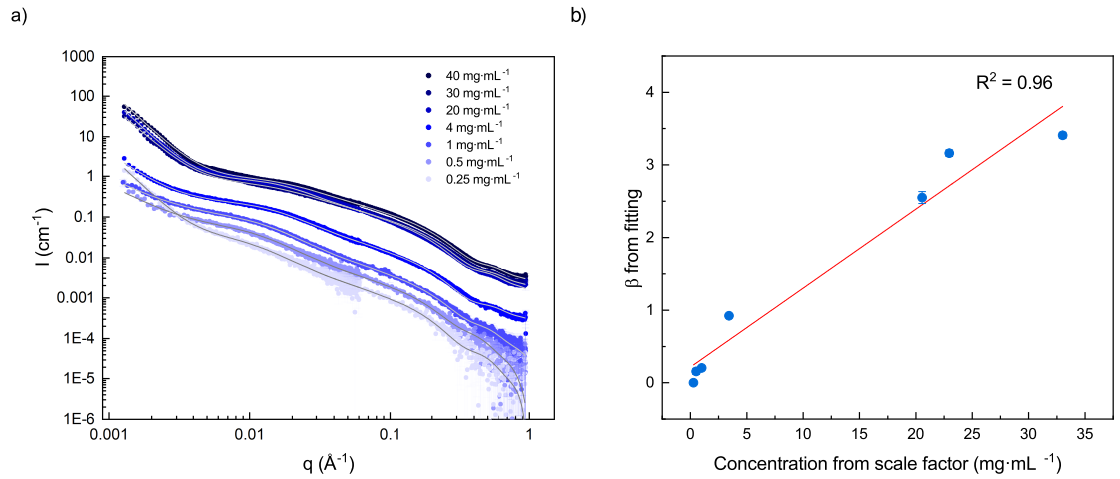

Figure 4.2: a) SAXS data of AX0.85 in water at different concentrations, and b) plot of β against concentration obtained from the scale factor. The red line is a linear fit where the slope $= 2MA_2$. Adapted from Janewithayapun, R. et al., *Carbohydrate Polymers*, 2025 under the CC-BY license.

observed as an increase in intensity at low q relative to concentration (Figure 4.3a-b). For AX0.57 at 20 mg·mL^{-1}, the intermediate q exponent is $\sim q^{-2.4}$, and the shoulder around $q = 0.01$ Å^{-1} is weakly observed. Then, when diluted to concentrations of 10, 4 and 1 mg·mL^{-1}, the intermediate q exponent decreases to $q^{-2.3}$, with no significant concentration dependence between the three lower concentrations.

For AX0.39 we observed steeper q decays of $q^{-2.75}$ in the intermediate q region for the 20 mg·mL^{-1} and 7.5 mg·mL^{-1} sample, than at 1 mg·mL^{-1} where a decay of $q^{-2.50}$ was observed (Figure 4.3b). The shoulder at $q = 0.01$ Å^{-1} is also less pronounced at 20 mg·mL^{-1} and stretches to lower q with a q^{-2} decay. The fact that lower chain compactness was observed only after dilution to 1 mg·mL^{-1} suggests that AX0.39 show the strongest tendency for aggregation of all three AX fractions.

The concentration dependent behavior of AX is strongly correlated to their substitution pattern. Highly branched AX scale similarly to polymer chains in good solvent environments, having repulsive interactions with other chains at higher concentrations. While those with more intermediate to low substitution show stronger tendency to aggregate. These behaviors are also in-line with the explanation of branching arabinose groups reducing inter-molecular interactions between AX chains [20, 21].

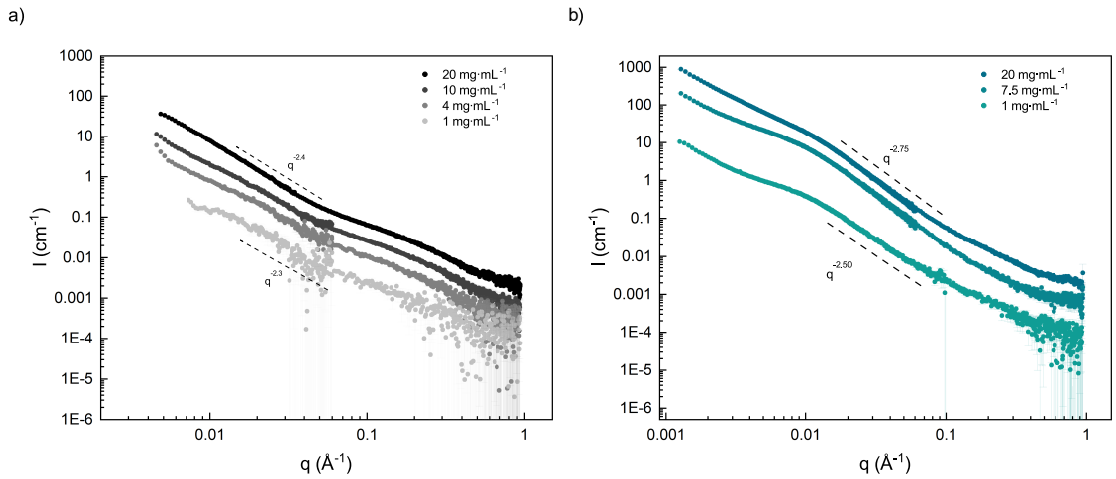

Figure 4.3: SAXS data from water dispersions of a) AX0.57, and b) of AX0.39 at different concentrations. Adapted from Janewithayapun, R. et al., *Carbohydrate Polymers*, 2025 under the CC-BY license.

4.2 Arabinoxylan conformation during and after ring-opening modification

In paper II, AX0.85 used in paper I was oxidized to produce dialdehyde AX (DAX) and dialcohol AX (DiolAX). The main objective of the experiments were to determine whether the chain conformation of AX changes after ring-opening modification. AX0.85 was chosen for this study because of their good solvent interaction with water as described in 4.1.

In-situ oxidation and time-resolved SAXS

SAXS data collected during in-situ periodate oxidation of AX to DAX is shown in Figure 4.4. An initial lower scattering intensity was observed for the first time point (reaction time, $t = 0$ min). This is due to the residual water in the tubing diluting AX at earlier measurement times.

The scattering features signficantly change with reaction time in the low q region, $0.005 < q < 0.02$ Å^{-1}. Taking the start of the reaction mixture arriving to the beam at $t = 0$ min, an increase in the steepness and intensity of the low q region was already observed at $t = 6$ min. The largest change in steepness and intensity at low q occurred between $t = 6$ min and $t = 9$ min, after which the increase of both parameters became more gradual. Given the lowest q measured in the time-resolved SAXS setup was 0.007 Å^{-1}, the lack of any observable Guinier plateau means that structures larger than 15 nm form with increasing reaction time (estimated from $qR_g < 1$. Inter-molecular hemiacetal bonds can form from oxidized dialdehyde groups [35, 98], as such, the rate of the increasing contribution of the low q slope is reflective of the rate of the inter-chain cross-linking reactions during the oxidation of AX.

In the intermediate q region between $0.02 < q < 0.1$ Å^{-1}, the scattering intensity is sensitive to changes in the chain conformation statistics such as the

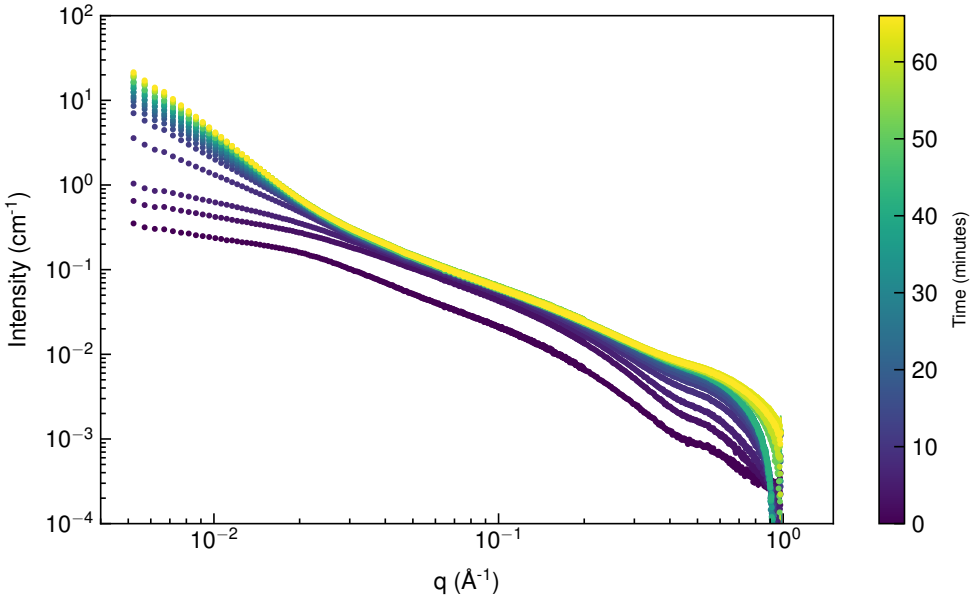

Figure 4.4: Time-resolved SAXS data of AX0.85 at a concentration of 20 mg $\cdot$ mL^{-1} in water during periodate oxidation with 0.5 equiv. of $NaIO_4$. SAXS scans were obtained from reaction time $t = 0$ min to $t = 66$ min at 3 min intervals.

Flory exponent (ν), as well as the L_p. At the concentration used in this in-situ experiment ($\sim$ 20 mg $\cdot$ mL^{-1}), AX is in the semi-dilute regime, and the chain conformation is affected by concentration, however, large variations in behavior should still be observable and assessed qualitatively. For instance, a decrease in L_p from 15 nm to 5 nm as in alginate [45], or a transition from an extended coil to a partially collapsed coil as in cellulose [44], should produce significantly different features in the SAXS data of AX. For AX, we find instead that the intermediate q region remains unchanged throughout the reaction.

The absence of changes in the intermediate q region means that no large changes in chain compactness or L_p occured during this oxidation of AX with 0.5 equiv. $NaIO_4$, which is close to the maximum obtainable DO for this branched AX.

Lastly, the high q ($q > 0.2$ Å^{-1}) features of the time-resolve scattering data exhibit increasing background level with time. We associate this to changes in solvent intensity variations coming from a $NaIO_4$ concentration gradient in the tubing.

Changes in the chemical structure of arabinoxylan with modification

The DO of the DiolAX reacted with 0.25 equiv. $NaIO_4$ was 21%, and the DO of the DiolAX with 0.5 equiv. $NaIO_4$ was 33%. These values were also

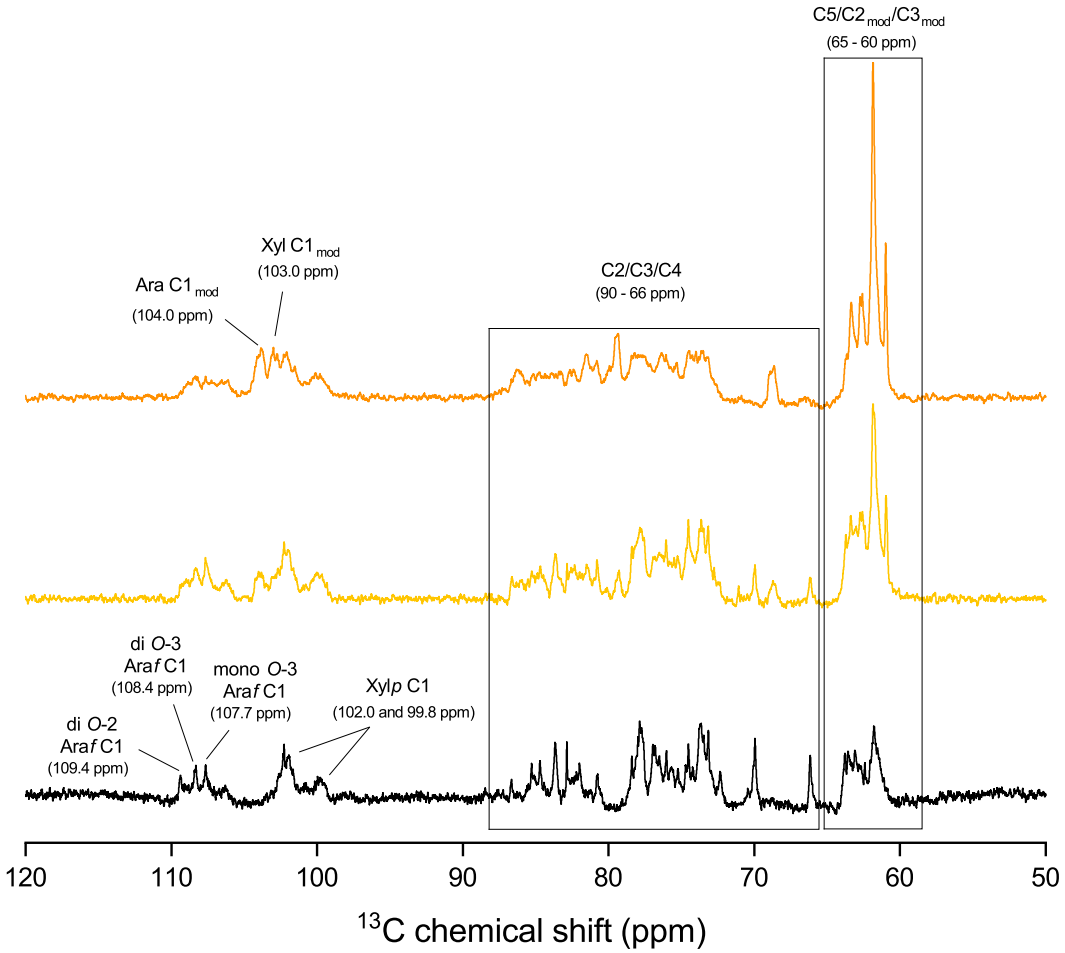

Figure 4.5: ^{13}C NMR spectra of DiolAX33 (orange), DiolAX21 (yellow) and AX (black) dissolved in DMSO-d6.

confirmed by solution state ^{13}C NMR in DMSO-d6. More details can be found in paper II. These samples will therefore be named DiolAX21 and DiolAX33, respectively. It is interesting to note that as $NaIO_4$ oxidation requires a viccinal diol for the reaction, only unsubstituted arabinose (Ara*f*) or xylose (Xyl*p*) monosaccharide residues can be oxidized. These would include t-Ara*f*, t-Xyl*p* and 4-Xyl*p*, accounting for a theoretical maximum DO of 48 mol% based on glycosidic linkage results (shown in the supplementary information of paper I, and in paper II).

The Xyl*p* C1 region and the Ara*f* C1 region can be assigned as shown in Figure 4.5. The Ara*f* C1 region contains three sharp peaks: at 107.7 ppm, 108.4 ppm and 109.4 ppm. The 107.7 ppm peak is assigned to mono-substituted *O*-3 Ara*f* C1, 108.4 ppm to di-substituted *O*-3 Ara*f* C1, and 109.4 ppm to a di-substituted *O*-2 Ara*f* C1 [99, 100]. The main Xyl*p* C1 peak is centered at 102.0 ppm, with another broad peak at 99.8 ppm. The latter is assigned to the Xyl*p* C1 of a di-substituted Xyl*p* unit (2,3,4-Xyl*p*) [99].

In the ^{13}C spectra of DiolAX21, there is a significant decrease in intensity of the di-substituted *O*-2 Ara*f* C1 signal at 109.4 ppm, along with a smaller decrease in intensity of the di-substituted *O*-3 Ara*f* C1 (108.4 ppm) signal.

The mono-substituted *O*-3 Ara*f* C1 (107.7 ppm) and the Xyl*p* C1 (102.0 ppm) signals remains unaffected. Hence, it appears that the periodate oxidation happens more predominantly on di-substituted Ara*f* groups. In addition to decreases in signal intensities, a new signal developed at 104.0 ppm, which we assign to ring-opened Ara*f* C1 units.

With increasing DO to DiolAX33, all three Ara*f* C1 signals decrease even further (Figure 4.5). No sharp peaks are observable in the 105 ppm to 110 ppm range. The evolution of the C1 region of the spectra across both DiolAX samples show that Ara*f* groups are oxidized most preferrably on di-substituted *O*-2 Ara*f* units, followed by di-substituted *O*-3 Ara*f*, and lastly the mono-substituted *O*-3 Ara*f*. Any Ara*f* units that can be oxidized are likely already ring-opened at this DO, therefore we assign the residual broad signals in this region to non-terminal Ara*f* residues (e.g. 2-Ara*f* or 2,5-Ara*f*) which would lack the vicinal diol groups required for periodate oxidation. For DiolAX33, there is also a small decrease in the Xyl*p* C1 signal at 102.0 ppm, and a new signal at 103.0 ppm, assigned to ring-opened Xyl*p* C1. The changes in the Xyl*p* signals, therefore indicate oxidation of Xyl*p* units as well at higher DO. Due to the more complex substitution pattern in high A/X ratio AX, there may be Xyl*p* units on the side groups that are oxidized as well, which would collaborate with smaller changes in A/X ratio for the highly branched AX after oxidation in paper IV.

Conformation of dialcohol arabinoxylan (DiolAX)

Dialcohol arabinoxylan (DiolAX), were prepared from the same AX0.85 batch. By adding a reduction step with $NaBH_4$, any dialdehyde groups in DAX, including the cross-linked functionalities are converted to dialcohol groups. DiolAX samples at degree of modification of 21% and 33% (DiolAX21 and DiolAX33) were studied to see whether larger alterations to the conformation can be observed close to the theoretical modification limit. We did not go above a DO of 15% for DAX as the amount of indispersible aggregates was already high at this DO.

The scattering features for both DiolAX21 and DiolAX33 were similar to each other, and to AX, as shown in Figure 4.6a-d. The main difference being the exponent and scale of the low q power law region.

Utilizing the same flexible cylinder model as for AX, the fitted L_p were obtained as 4.0 nm and 3.9 nm for DiolAX21 and DiolAX33, respectively. Therefore, the reduction in L_p was approximately 10% between AX and DiolAX33.

The fitted value for the contour length and the intensity at zero q, $I(0)$ were similar between AX, DiolAX21 and DiolAX33 ($\pm$12%), suggesting that no major M_w decrease has occurred in these samples. Typically, in oxidation-reduction, a decrease in M_w is to be expected as a result of chain scission side reactions during oxidation [32] and elimination reactions during reduction [101]. This could be largely affected by the purification of DiolAX samples

through dialysis with a 3.5 kDa membrane cutoff, which would have removed any degraded short chains.

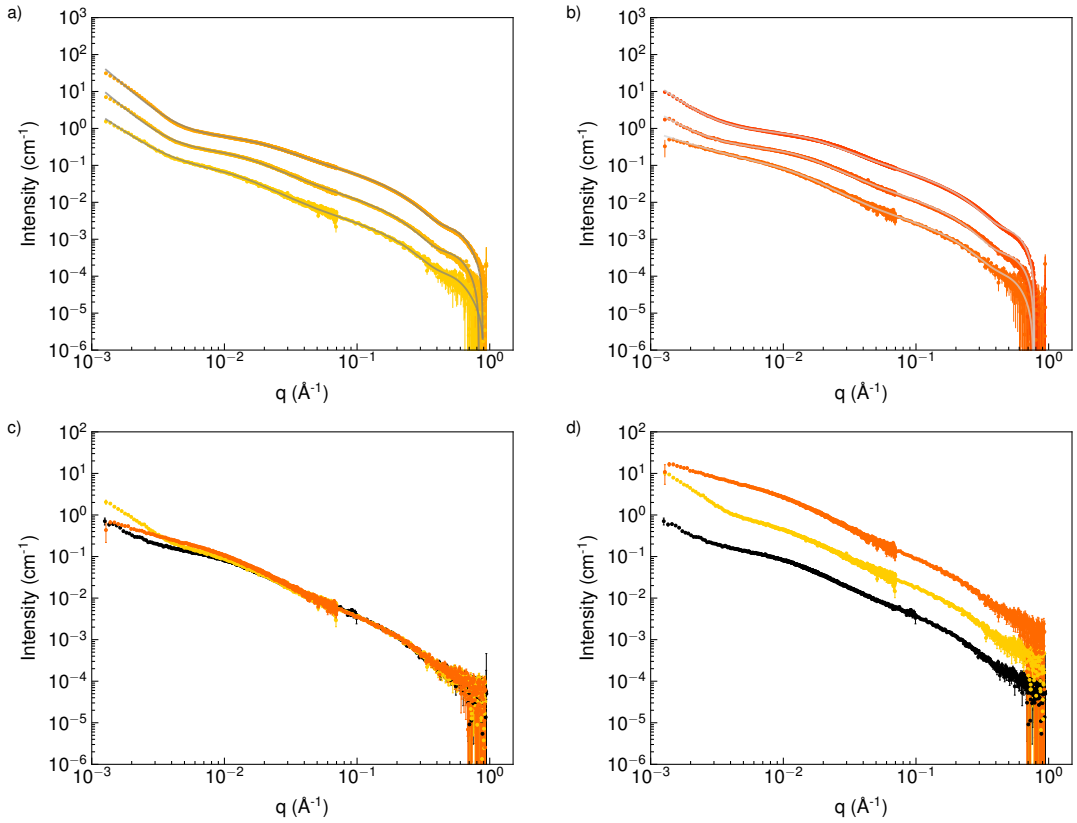

Figure 4.6: a) DiolAX21, and b) DiolAX33 at concentrations of 1 mg $\cdot$ mL^{-1}, 4 mg $\cdot$ mL^{-1} and 20 mg $\cdot$ mL^{-1}, with lines showing fit to a flexible cylinder model. c) Comparisons of AX (black), DiolAX21 (yellow) and DiolAX33 (orange) at 1 mg $\cdot$ mL^{-1}, d) DiolAX21 data was shifted by a factor of 5, and DiolAX33 by a factor of 25 for ease of viewing.

From analysis of the concentration series for DiolAX, the structure factor and its fitted parameter β was obtained for DiolAX21 and DiolAX33 (Figure 4.7). The slope of the plot of β against concentration gives $2MA_2$, assuming similar M for all three materials, A_2 of DiolAX21 would be similar to AX, and lower for DiolAX33, indicating lower solvent quality for the DiolAX33, although all three materials are still in the good solvent regime. The decrease in solvent quality at the highest degree of oxidation could be a result of a lowered steric hindrance for chain interactions that is provided by arabinose side groups [21].

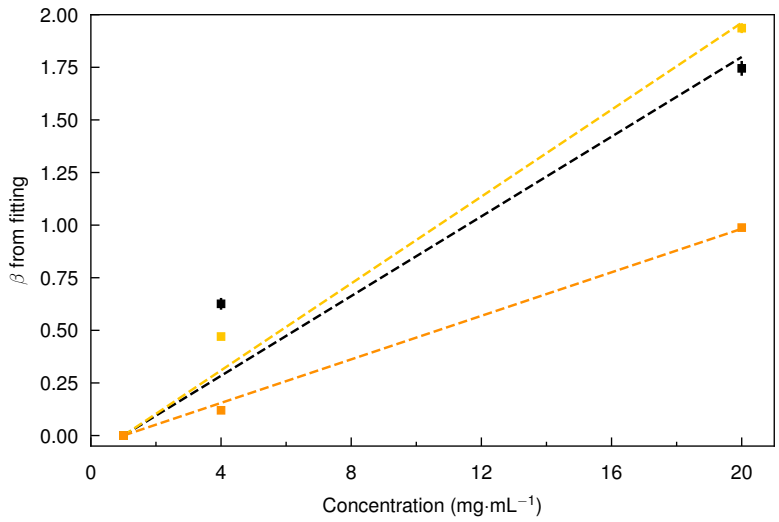

Figure 4.7: Fitted values of β against concentration for AX (black), DiolAX21 (yellow) and DiolAX33 (orange), where $\beta = 2MA_2c$. Dashed lines show the linear fit of the data points.

Summary of the investigation of arabinoxylan and derivatives in solution and dispersion

AX with higher A/X ratios adopt more extended conformations in water. Variations were observed in both the L_p, and the statistical conformation of the chains. From the investigation on the structural changes of AX, DAX and DiolAX in solution and dispersion, we conclude that ring-opening of the soluble highly branched AX0.85 results in small changes on L_p (on the order of $\pm 10\%$), chain conformation statistics, and scaling with concentration. Based on chemical characterizations of the DiolAX, we see that ring-opening happens faster, and with preferrence for the arabinose sidegroups. It therefore follows, that backbone modification which would have the largest impact on the chain conformation, had not occurred to a large extent, compared to, for example, more linear polysaccharides such as cellulose or alginate [44, 102].

4.3 Structures of arabinoxylan in the solid-state

The structure of solid AX films with high and low A/X was studied, so that the effects of butyl glycidyl ether (BGE) etherification on the nano-structure of AX can be studied. The resulting WAXS intensity data is shown in Figure 4.8. Different fractions of high and low A/X were used here than in paper I and II, the AX fractions used in paper IV are referred to as AX0.9, AX0.5 and AX0.3, in order of high to low A/X.

AX0.9 exhibits amorphous peaks, consisting of a broad peak above 2 $Å^{-1}$, associated to intra-chain correlation lengths [63], followed by peaks at around 1.4 $Å^{-1}$ and 0.7 $Å^{-1}$. These latter two should represent monomer-monomer distances, and or inter-chain distances. Similar amorphous peaks can be observed in AX0.3, with a peak at 0.9 $Å^{-1}$ instead of 0.7 $Å^{-1}$. This supports the assignment of the lowest q peak of the WAXS data to that of inter-chain distances, which would be larger for a more highly branched AX. In addition to amorphous peaks, AX0.3 showed sharper contributions from crystalline regions matching with those of xylan crystallite diffraction planes q values of 0.89 $Å^{-1}$ ($2\theta = 12.4°$, 101 & 011), and at a q value of 1.38 $Å^{-1}$ ($2\theta = 19.1°$, 110) [27].

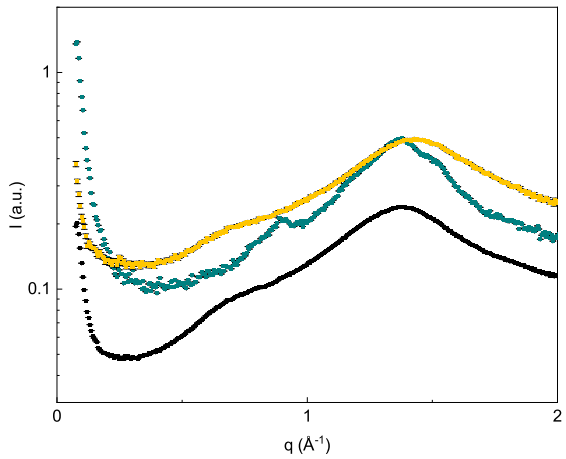

Figure 4.8: WAXS data of AX0.9 (black), AX0.3 (green) and DiolAX25 made from AX0.9 (yellow)

Structure of modified AX derivatives

The WAXS intensity of AX0.9 and its DiolAX25 (degree of modification 23%) is shown in Figure 4.8. The amorphous peak around 1.4 $Å^{-1}$ shifts slightly to higher q in DiolAX which may be indicative of changes in monomer repeating distances as a result of the ring-opening, but overall there were no large changes in the observed atomic-scale structure.

The structure of butyl glycidyl etherified derivatives showed larger differences in the WAXS scattering intensity features, shown in Figure 4.9a. At low q (< 0.1 $Å^{-1}$), q-decays of q^{-2} for BGE-DiolAX0.3, and q^{-3} for BGE-DiolAX0.9 and 0.5 were observed. The q^{-3} decay could be from defects and voids on a nanoscale occurring from the melt-compression of films [72, 103, 104], while the shift to a q^{-2} decay in the BGE-DiolAX0.3 film is expected to be a result of larger structure inhomogeneities. At high q, amorphous peaks representing atomic scale distances were present at similar q to AX and DiolAX. A new feature in all BGE-DiolAX films is the prominent peak at ~ 0.2 $Å^{-1}$. For BGE-DiolAX0.3 and BGE-DiolAX0.90, the peak is centered at 0.18 $Å^{-1}$, and for BGE-DiolAX0.5 at 0.23 $Å^{-1}$. These peaks correspond to real space distances of 35 Å and 27 Å, respectively. The hypothesis is that the space distances

originate from aggregation and formation nano-sized domains consisting of side chain rich regions on one side, and of AX backbone rich regions on the other. No clear trend could be drawn between the nano-domain size and AX branch density of the materials however, BGE-DiolAX0.5 had a smaller nano-domain size, while BGE-DiolAX0.9 and BGE-DiolAX0.3 had similar nano-domain size despite being the two most different AX, composition wise.

BGE-DiolAX0.3, shows further sharp peaks at 1.50 $Å^{-1}$ and 0.12 $Å^{-1}$ in the WAXS curve, and at 1.70 $Å^{-1}$ in XRD measurements (Figure 4.9b), these peaks do not match with those of a xylan crystallite [27]. It was also observed that the peak at 0.12 $Å^{-1}$ becomes more pronounced upon melt compression and disappears when heated above 80 °C. The peak at 1.70 $Å^{-1}$ corresponds to a real space distance of 3.7 Å and could represent small degrees of lateral crystallization within the BGE side chains. The peak centered at 0.12 $Å^{-1}$ has a real space distance of 52 Å, and is affected by temperature, hence we assign it to ordered regions on the length scale of the nano-domains.

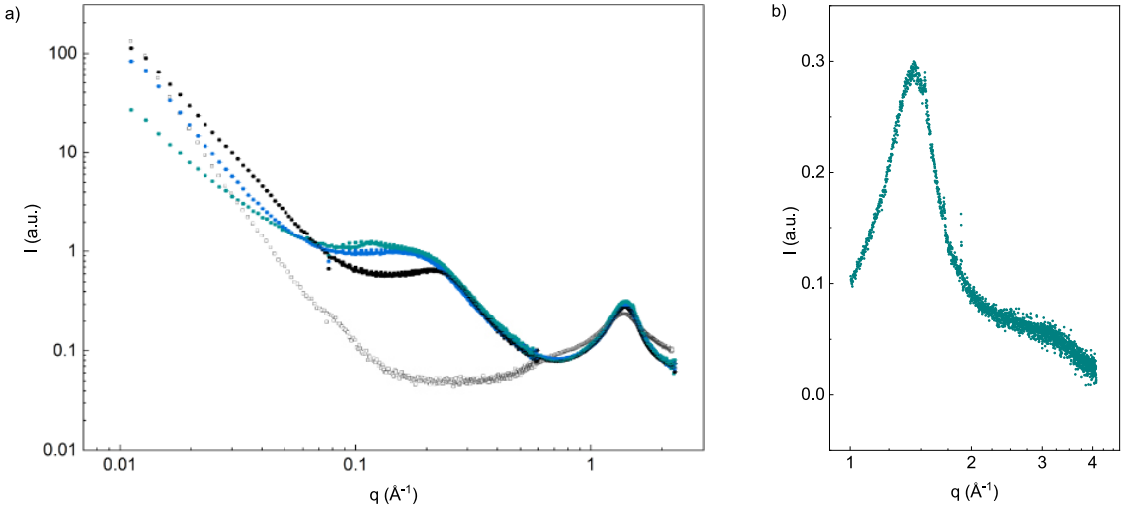

Figure 4.9: a) Combined SAXS and WAXS data for BGE-DiolAX0.3 (green), BGE-DiolAX0.5 (black), BGE-DiolAX0.9 (blue), and AX0.9 (open symbol, black), b) XRD data for BGE-DiolAX0.3. Adapted from Janewithayapun, R. et al., *Carbohydrate Polymers*, 2024 under the CC-BY license.

On the microscopic and macroscopic scale, differences in structures were also observed between the films. When BGE-DiolAX0.3, 0.5 and 0.9 were compression molded into films of 0.1 mm thickness, BGE-DiolAX0.3 showed microscopic birefringent regions, indicating the presence of larger ordered structures, while films of BGE-DiolAX0.5 and 0.9 did not contain birefringent regions (Figure 4.10). Similarly, on the macroscopic scale inhomogeneities were observed as opaque clusters on the BGE-DiolAX0.3 film (Figure 4.11a), while the films of BGE-DiolAX0.5 and BGE-DiolAX0.9 were clear and transparent (Figure 4.11b-c), indicating homogeneity on the macroscale for the latter two. When heated to around 85 °C on a Kofler bench (long heating plate with temperature gradient), the large opaque clusters on BGE-DiolAX0.3 disappear almost completely, but the film still has an inhomogeneous, macroscopically

phase separated appearance. It should be noted that the textures observed on all films are a result of patterns on the Teflon sheet used during compression molding.

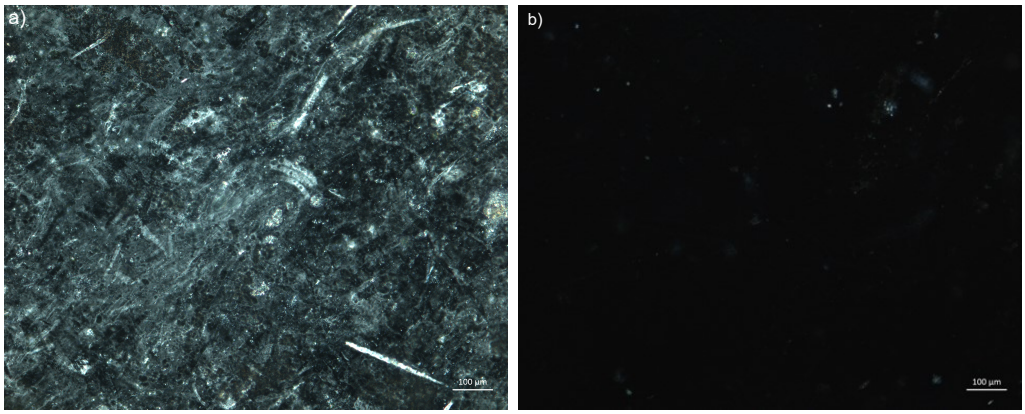

Figure 4.10: Polarized light microscope images of compression molded films from a) BGE-DiolAX0.3, and b) BGE-DiolAX0.9. Scale bars show 100 µm.

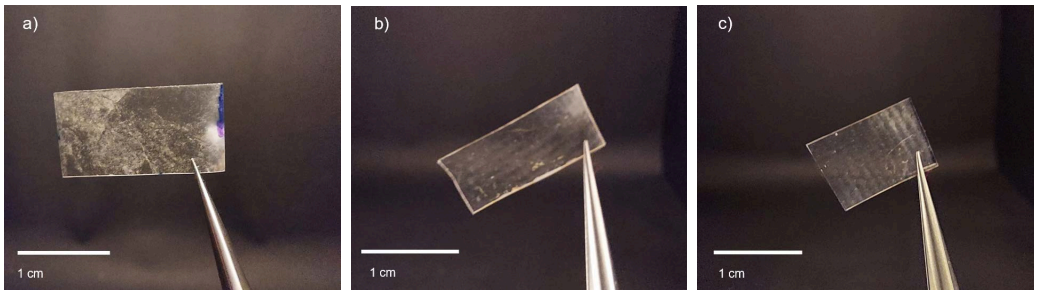

Figure 4.11: Images of compression molded films from; a) BGE-DiolAX0.3, b) BGE-DiolAX0.5, and c) BGE-DiolAX0.9, with thickness of 0.1 mm. Reproduced from Janewithayapun, R. et al., *Carbohydrate Polymers*, 2024 under the CC-BY license.

In branched nanophase separated poly(n-alkyl acrylates), the alkyl domains are flexible and also serve as a form of internal plasticization, lowering $T_{g,\alpha}$ of the chain [105]. On the other hand, the stiffer main chains separating the mobile alkyl domains contribute rigidity to the material when below $T_{g,\alpha}$.

We reason that the same behavior extends to BGE-DiolAX, the BGE domains are flexible, and separates the AX backbone, reducing the intermolecular interactions between AX chains, both of which contribute increased mobility in the system. We see from the solution state experiments that the AX chains are stiff, even when oxidized to DiolAX. Hence, they act as the rigid spacers between BGE domains.

A separate case can be considered for AX0.39 (paper I), and the similar AX0.3 (paper IV), both of which have similar A/X ratio. AX0.39 had a shorter persistence length (L_p) in solution and showed strong aggregation tendencies.

The behavior is similar for AX0.3 in the solid state, which formed crystalline regions. The modification of these materials likely proceed differently, with reactions occurring more on the surfaces of the aggregates. This may have resulted in the ordered structural features in BGE-DiolAX0.3, and through that, affect their macromolecular properties. These ordered structures are suggested as explanations for the higher Young's modulus, as the ordered structures can hinder the mobility and sliding of the chains under strain (Figure 4.12). The ordered structures can also act as fracture initiation points, leading to the low strain at break observed in tensile testing. Similar results were observed in studies on alkyl celluloses, where lowered ductility was observed when ordered structures were found in the side chains [52].

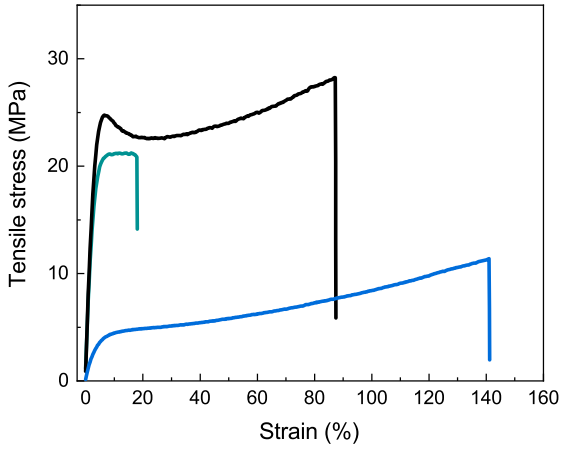

Figure 4.12: Tensile testing stress strain curves of BGE-DiolAX0.3 (green), BGE-DiolAX0.5 (black), and BGE-DiolAX0.9 (blue). Reproduced from Janewithayapun, R. et al., *Carbohydrate Polymers*, 2024 under the CC-BY license.

4.4 Dynamics of arabinoxylan

Unmodified AX does not soften to a large extent when heated, hence, it cannot be compression molded. A solvent casted film of AX0.9 does display some relaxation behavior in DMA with temperature: at approximately 0 °C, 50 °C and 100 °C (Figure 4.13), but the storage modulus (E') remains high at around 800 MPa at 125 °C. When measured with dynamic scanning calorimetry (DSC) , no transitions were observable up to 125 °C [10]. This is in agreement with previous work by Börjesson et al. [42], showing that AX does not soften considerably until above 200 °C, when E' falls to around 100 MPa. However, thermogravimetric measurements show that AX begin to degrade at 200 °C under N_2 flow [10], thus melt processing is not possible for unmodified AX. Börjesson et al. [42] further showed that no large changes in DMA results were observed for oxidized AX either, therefore, in this thesis, characterization methods that may be more sensitive to faster dynamics at the molecular scale such as NMR and neutron spectroscopy were used.

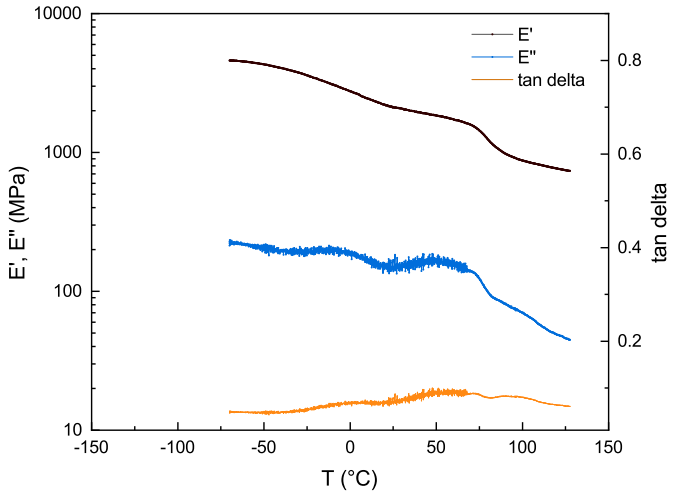

Figure 4.13: E', E'' and tan delta of a solvent casted AX0.9 film collected at a frequency of 1 Hz, amplitude of 8 µm (approximately 0.05% strain), and heating rate of 3 °C · min^{-1}.

4.5 Dynamics of arabinoxylan after ring-opening modification

CP/MAS with variable contact time experiments

The dynamics of AX0.9, and its derivatives dialdehyde AX (DAX23) and dialcohol AX (DiolAX25) were studied with solid-state NMR in manuscript III. During cross-polarization, the intensity at contact time t can be written as shown in Equation 2.2. By measuring the ^{13}C integral intensity as a function of contact time, the mobility of protons in the vicinity of the carbon environment can be studied. A plot showing the decay in intensity such as in Figure 4.14 can be made and from the data, the proton relaxation in the rotating frame $T_{1\rho H}$ and the CP time constant T_{CH} can be fitted. Considering data from side chain grafted BGE-DiolAX, which is discussed in a later section, we conclude that dynamics of the AX main chain falls into the slow regime shown in Figure 2.9, hence a decrease in $T_{1\rho H}$ indicates more and/or faster molecular motions. While that of the BGE side chains fall into the fast regime where the opposite occurs.

For the samples stored at 53% RH, the moisture uptake measured by DVS were 10% wt., 11% wt. and 11% wt. for AX, DAX23 and DiolAX25, respectively. The integral of all carbon environments in DiolAX25 show faster decay in intensity compared to AX (Figure 4.14). For C1, the $T_{1\rho H}$ of DiolAX25 was lower by a factor of 2 - 2.3 compared to AX. The $T_{1\rho H}$ of DAX23 was larger than that of AX for all carbon signals by a factor of 1.3 to 1.5, likely due to cross-linking (Figure 4.14b). As the choice of NMR sequence did not allow for good resolution of the initial build-up, the errors for the fitted T_{CH}may be large, and detailed interpretation was not done on it.

Such large differences in $T_{1\rho H}$ were not observed in the sample stored at 20 % RH. The decay of the C1 integrals show a similar decay rate for AX, DAX23

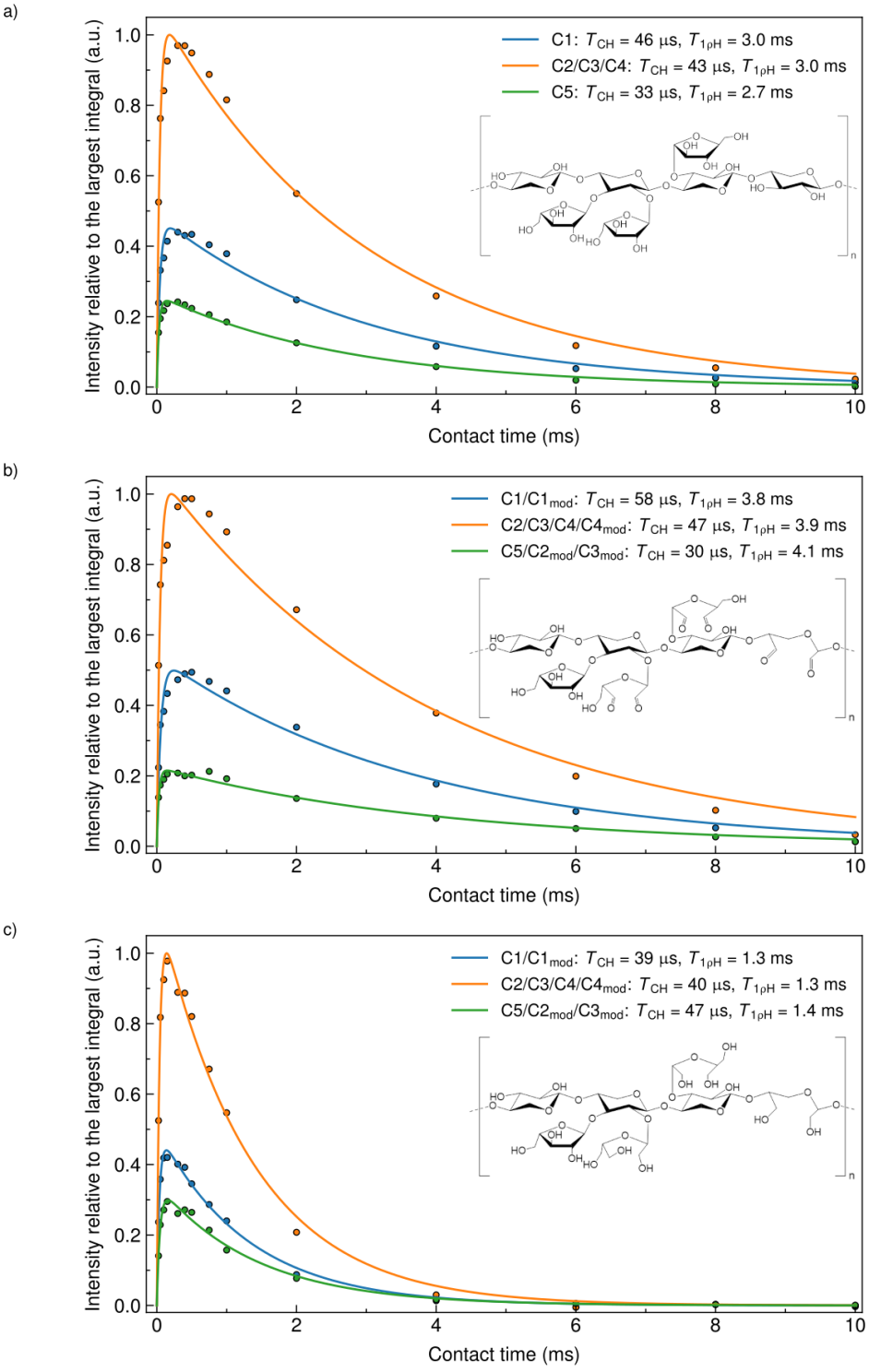

Figure 4.14: CP/MAS integral of samples equilibrated at 53% RH as a function of CP contact time for a) AX, b) DAX23, and c) DiolAX25. Integration regions show: C1/C1$_{\mathrm{mod}}$ (114.8 - 98.8 ppm), C2/C3/C4/C4$_{\mathrm{mod}}$ (92.8 - 66.5 ppm) and C5/C2$_{\mathrm{mod}}$/C3$_{\mathrm{mod}}$ (66.5 - 56 ppm) in blue, orange and green, respectively.

and DiolAX25 (Manuscript 3, Figure S3, supplementary information). The value of $T_{1\rho H}$ fitted for AX were larger by factors 1.4 to 1.5. For DiolAX25, $T_{1\rho H}$ was larger by factors of 2 to 2.4. Interestingly, the $T_{1\rho H}$ of DAX23 were

not significantly changed, in fact, the fitted $T_{1\rho H}$ were slightly lower for the samples stored at 20 % RH.

The lower $T_{1\rho H}$ of DiolAX25 indicates that there is an increase in molecular motions compared to AX and DAX23, with correlation time in the range 10 kHz to 100 kHz (100 µs to 10 µs) [74, 75]. Furthermore, as seen from the larger $T_{1\rho H}$ for DiolAX25 20 % RH, these motions are reduced at lower moisture contents, demonstrating the plasticization effect of water on these two materials. Interestingly, DAX23 was not affected, possibly due to the cross-linked functionalities formed from the dialdehyde groups. Plasticization has been shown to increase free volume in polymer chains, and disrupts intermolecular hydrogen bonding, both of which facilitate bond rotation and chain mobility [106]. Therefore, it can be reasoned that the ring-opened sections in DiolAX25 are indeed more mobile than AX or DAX23, but mobility is hindered until plasticized at a certain moisture content. $T_{1\rho H}$ is affected by spin diffusion [74], hence all carbon signals in DiolAX25 share similar $T_{1\rho H}$ and we cannot individually analyze their dynamics from $T_{1\rho H}$.

2D ^{1}H-^{13}C wideline-separation NMR experiments

The mobility of the different carbon environments of AX and derivatives were further studied with the 2D WISE experiment. Large-amplitude motions faster than the dipolar coupling (50 kHz) lead to a reduction of the proton dipolar line width [82], allowing a qualitative comparison of mobility to be made by comparing the proton linewidth associated with each carbon resonance. Radloff, Boeffel and Spiess [83] showed that sharp water signals were not detected in the linewidth of cellulose at short mixing times (mixing time of 0 ms and CP time of 2 ms), as there was insufficient time for spin diffusion between water protons and cellulose aliphatic protons. Only at a mixing time of 5 ms were water signals observed. Therefore, in our WISE experiment with a CP time of 0.3 ms, and a mixing time of 0.01 ms, the spectra should be dominated by signals from the CH and CH_2 groups [83].

The WISE 2D plots for the shortest mixing time experiments for the three materials stored at 53% RH are shown in Figure 4.15a-c. The linewidth of AX and DAX23 are broader than DiolAX25, with full width at half maximum (FWHM) of 44-49 kHz and 36-37 kHz respectively. The broader signals agree with measurements on cellulose [83] and shows that the polymer backbone of AX and DAX23 are immobile. On the other hand, the spectra of DiolAX25 show a sharper peak in the C5/$C2_{mod}$/$C3_{mod}$ region (56 - 66.5 ppm) with a FWHM of 17 kHz. The other peaks in DiolAX25 are broader, with FWHM of around 25 kHz to 26 kHz. The narrower linewidth of C5/$C2_{mod}$/$C3_{mod}$ point towards a higher prevalence of motions associated with these carbon environments in DiolAX25, which is in agreement with the larger value of T_{CH} obtained from the CP/MAS experiments. We would also reason that the motions are more likely associated to the ring-opened $C2_{mod}$ and $C3_{mod}$, rather than the unmodified C5. With increasing mixing time to 1 ms and 2.5 ms, AX and DAX23 exhibited a narrowing of the linewidth as a result of spin diffusion from mobile water, similar to that observed in cellulose [83]. The linewidth of

DiolAX25 showed some narrowing, but to a much smaller extent (Manuscript III, Figure 6). The mobility observed in DiolAX25 at a mixing time of 0.01 ms can therefore be safely attributed to an actual increased mobility in the DiolAX25 polymer chain.

For the samples stored at 20 % RH, the linewidth of DiolAX25 in the $C5/C2_{mod}/C3_{mod}$ region broadens (Figure 4.15d), with similar linewidths to AX or DAX23 at 53% RH in Figure 4.15a-b. These results are in agreement with the larger $T_{1\rho H}$ and T_{CH} from CP/MAS, and show that the increased mobility in DiolAX25 are not observed at low moisture contents.

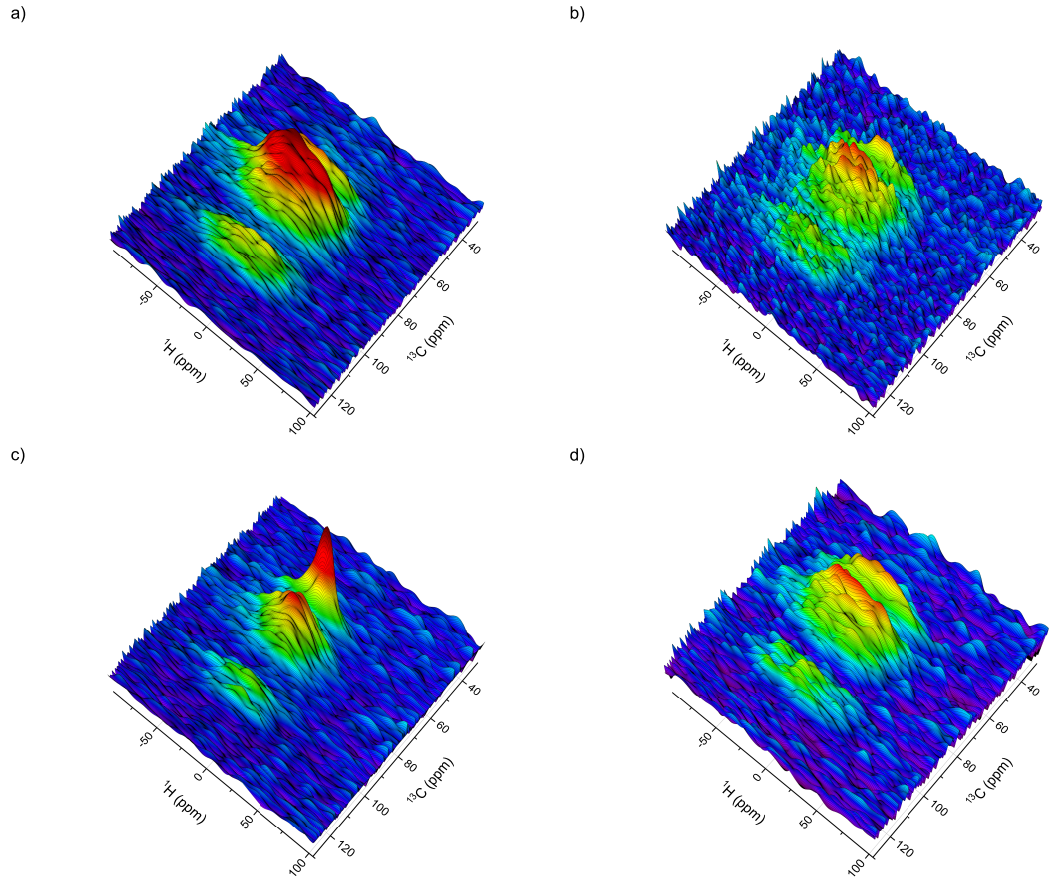

Figure 4.15: 2D WISE NMR spectra with CP time = 0.3 ms, mixing time = 0.01 ms, of a) AX 53% RH, b) DAX23 53% RH, c) DiolAX25 53% RH, and d) DiolAX25 at 20 % RH.

Quasielastic neutron scattering fixed window scans

Measurements of FWS intensities by QENS provide an overview of the changes in dynamics of the system [88]. The elastic intensity shown in Figure 4.16, decreases more steeply for DiolAX compared to AX above $\sim$ 280 K and is accompanied by a steeper increase in the inelastic intensity at 3 µeV. Note that the bump in the elastic intensity of DiolAX25 at 230 K is attributed to a measurement artifact. Motions within the sample lead to energy transfer between the probe neutrons and the sample, resulting in a decrease in the elastic

intensity and an increase in the inelastic intensity. An energy transfer of 3 µeV corresponds to motions on the ns timescale [88]. Above 280 K, contributions mainly come from the motions of the polysaccharide chains, rather than any residual water in the sample which have much faster correlation times [107].

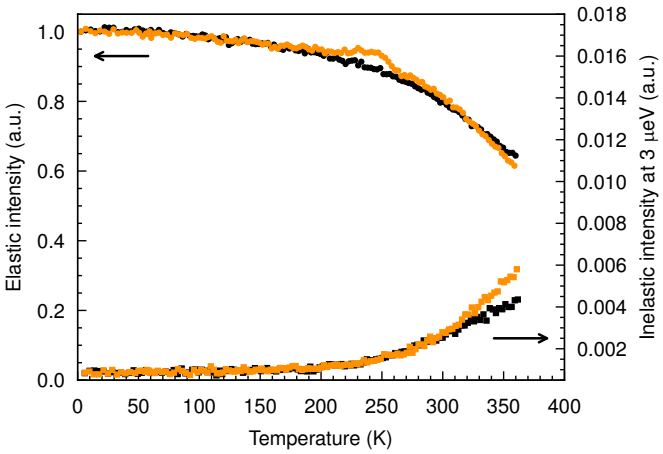

Figure 4.16: Elastic fixed window scan data collected from IN16b for AX0.9 (black) and DiolAX25 (orange) stored at 53% RH D_2O.

In summary, increased molecular motions were observed when AX was oxidized and reduced to the ring-opened DiolAX25 with a DO of 25%. This was seen through a two- to three-fold decrease in $T_{1\rho H}$ obtained from a CP/MAS experiment with variable contact time, for DiolAX25 compared to AX and DAX. The mobility was observed only in the DiolAX25 stored at 53% RH (moisture content of 10.8 wt.%), showing the significant role of water as a plasticizer. Through the WISE experiments, we were able identify narrow proton linewidths for DiolAX25 at 53% RH in the C5/$C2_{mod}$/$C3_{mod}$ region, whereas broader peaks were observed for all other carbon signals and samples. As narrowing of the proton linewidth can be linked to increased molecular motion, the observed narrow linewidths point specifically towards higher mobility in the ring-opened $C2_{mod}$,$C3_{mod}$ of DiolAX25. QENS FWS data corroborate the findings from solid-state NMR, showing increased dynamics in DiolAX compared to AX.

4.6 Dynamics of etherified arabinoxylan and dialcohol arabinoxylan

CP/MAS with variable contact time experiments

The last step in the modification sequence consists of an etherification of DiolAX with butyl glycidyl ether (BGE). The same solid-state NMR experiments as in the section above were performed for BGE-DiolAX0.9. The material has a degree of BGE substitution (DS) of 1.1 by ^{1}H NMR of the acid hydrolysate [10]. The CP/MAS relaxation behavior is shown in Figure 4.17. Some overlap

occurs between C2-4 of the DiolAX and the BGE signals coming from more deshielded carbon environments where the glycidyl groups were, and is taken into consideration during data analysis. From Figure 2.9, it is apparent that the BGE signals at 14.6 ppm, 19.9 ppm and 32.3 ppm decay much slower than those of the DiolAX signals at higher ppm with CP contact time, indicating different correlation times for the side chain and main chain motions. In the motion regimes described in Figure 2.9, the BGE side chain is expected to be in the fast regime, therefore, when $T_{1\rho H}$ and T_{CH} was fitted, larger values were obtained compared to DiolAX. The fitted $T_{1\rho H}$ for the DiolAX C1 component of BGE-DiolAX0.9 is similar to that of DiolAX25, indicating that the mobility of the DiolAX segment from ring-opening is still in effect after etherification. The moisture uptake of BGE-DiolAX0.9 was lower (6% wt.) than DiolAX25 (11% wt.), which may have contributed to the difference.

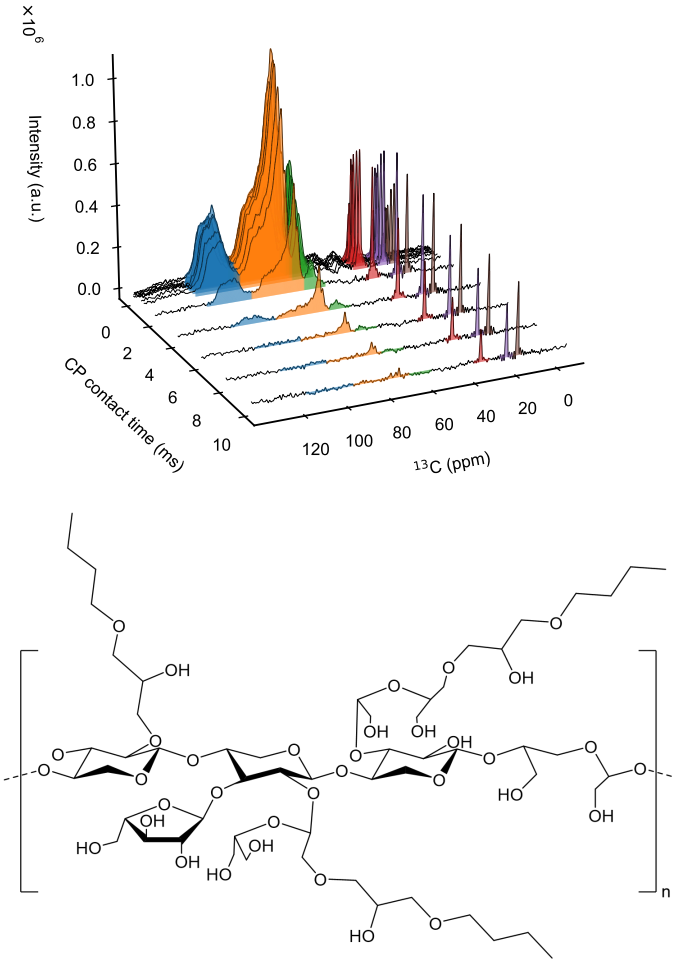

Figure 4.17: 3D plot of ^{13}C intensity as a function of CP contact time for BGE-DiolAX0.9 at 53% RH.

When BGE-DiolAX0.9 was equilibrated at low humidity, $T_{1\rho H}$ increased for the DiolAX signals, and decreased for the BGE side chain signals. This behavior is logical and support our assignment of DiolAX chain segments

to be in the slow motion regime, and BGE side chains in the fast motion regime. At low moisture content, all motions are slower, hence $T_{1\rho H}$ should increase for motions in the slow regime and decrease for those in the fast regime Additionally, this shows that the BGE-DiolAX0.9 chains are still plasticized by water despite its increased hydrophobicity.

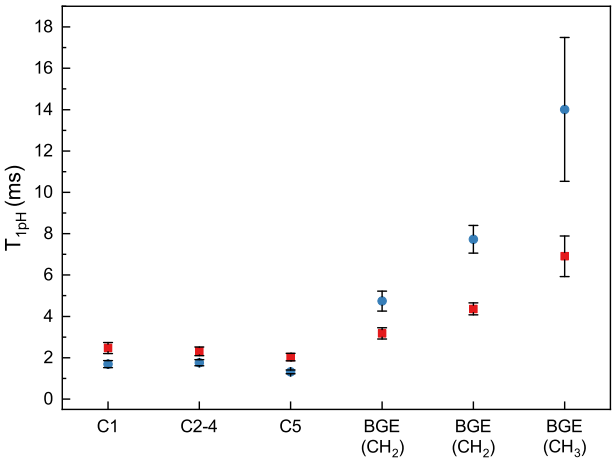

Figure 4.18: $T_{1\rho H}$ for ^{13}C signals in BGE-DiolAX0.9 at 53% RH (blue) and at 20 % RH (red).

Comparisons between BGE-DiolAX and BGE-AX

In order to assess the effect of ring-opening on etherified AX materials as well, a control material from etherified AX0.9, without ring-opening was made: BGE-AX0.9. Another batch of BGE-DiolAX0.9 was also synthesized, to have a similar degree of substitution (DS) to the control. The solution ^1H NMR spectra of both materials are shown in Figure 4.19. The two spectra have been scaled to be similar in intensity in the AX region (3 ppm to 5 ppm) and qualitatively, we assess that the two materials share a comparable DS. As the intensities of the BGE signals in the shaded region are lower compared to the ^1H NMR spectra of previous materials, we also know that the DS is below 1. A quantitative integration is difficult due to overlapping peaks between AX and BGE in the polysaccharide spectra, and a better comparison can be made by NMR of acid hydrolysates after all experiments have finished.

The two materials; BGE-DiolAX0.9 and BGE-AX0.9 were studied with QENS on three different instruments to have a wider energy transfer range. The elastic FWS and inelastic FWS ($\omega = 3$ μeV) scans are analyzed first, as they provide a quick overview of the system. From Figure 4.20, materials with BGE show two clear transitions, one centered around 200 K, and another that has an onset at 260 K but does not show a peak in the measured temperature range (up to 360 K). The transition at lower temperature originates from the BGE side chains, and contributes to a larger decrease in the elastic intensity for BGE-DiolAX0.9 than BGE-AX0.9. Also interesting, is the slope of the higher temperature transition. The increase in inelastic intensity of DiolAX25 and BGE-DiolAX0.9 share very similar slopes above 260 K. Furthermore, AX0.9

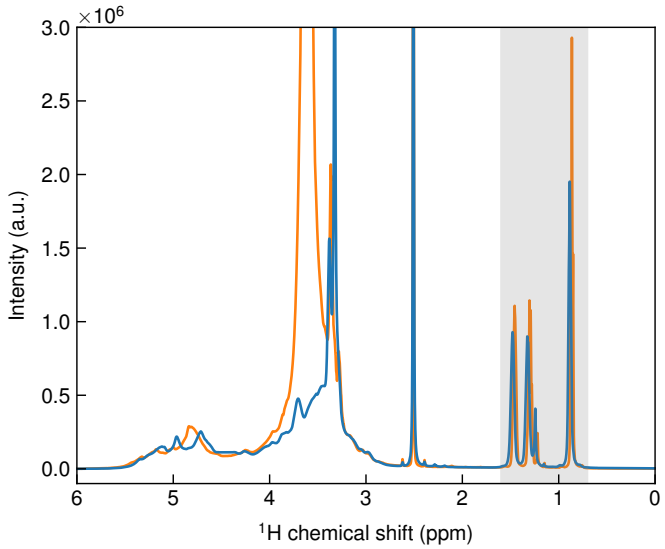

Figure 4.19: ^{1}H NMR spectra of BGE-DiolAX0.9 (orange) and BGE-AX0.9 (blue) in DMSO-d6. BGE CH_3 (0.9 ppm) and CH_2 groups (1.5 ppm and 1.3 ppm) are indicated by the gray area.

and BGE-AX0.9 also match well in slope for inelastic intensity above 260 K. The FWS provides a good estimate for the number of different dynamics in the system [88], and also imply that the ring-opened AX retains similar main chain motions even after etherification.

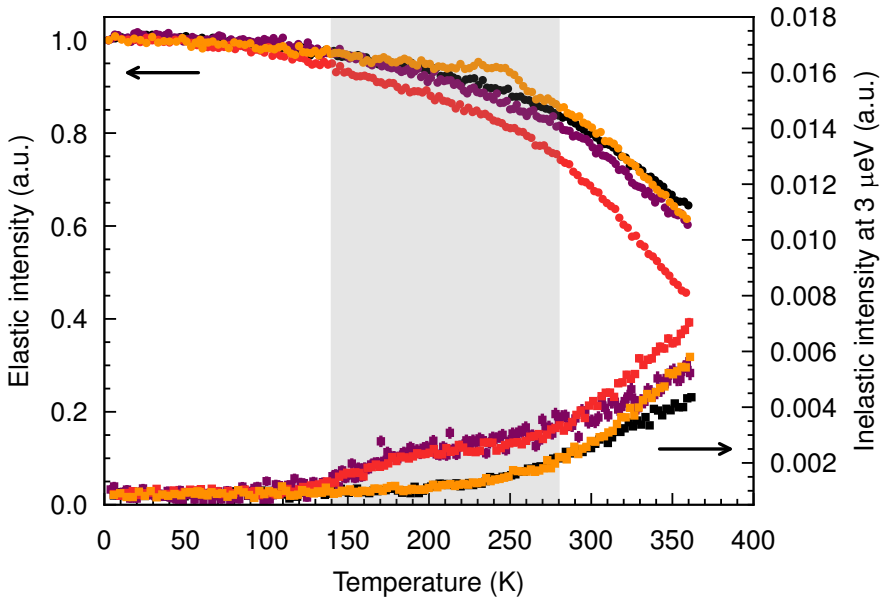

Figure 4.20: Plot of the elastic intensity and inelastic intensity at 3 μeV as a function of temperature for AX0.9 (black) and DiolAX25 (orange), BGE-AX0.9 (purple) and BGE-DiolAX0.9 (red) kept at 53% RH (D_2O). Shaded region highlights the different motion onsets discussed. The data was summed over all q ranges and normalized by the elastic intensity at 2 K.

QENS spectra at 360 K ($q = 0.95$ Å^{-1}) measured on IN16b for the four materials are shown in Figure 4.21. From the data the two BGE containing samples show more broadening than the DiolAX25 or AX0.9. Note that the flat background has higher contributions in BGE-AX0.9 than BGE-DiolAX0.9 due to samples transmission differences, hence care must be taken when qualitatively comparing them. In the region closer to the elastic line ($\omega < 5$ μeV), as shown in Figure 4.21b, there is a higer intensity of the broadening close to the elastic line for BGE-DiolAX0.9, indicating a larger contribution from slower motions, matching with what was observed in the FWS data. Data collected on SHARPER and OSIRIS are shown in Figures 4.21c-d and show other motions present with higher energy transfers (and therefore correlation times). Future fitting of the collected data should provide more insights into the activation energy, confinement and intensity of the motions.

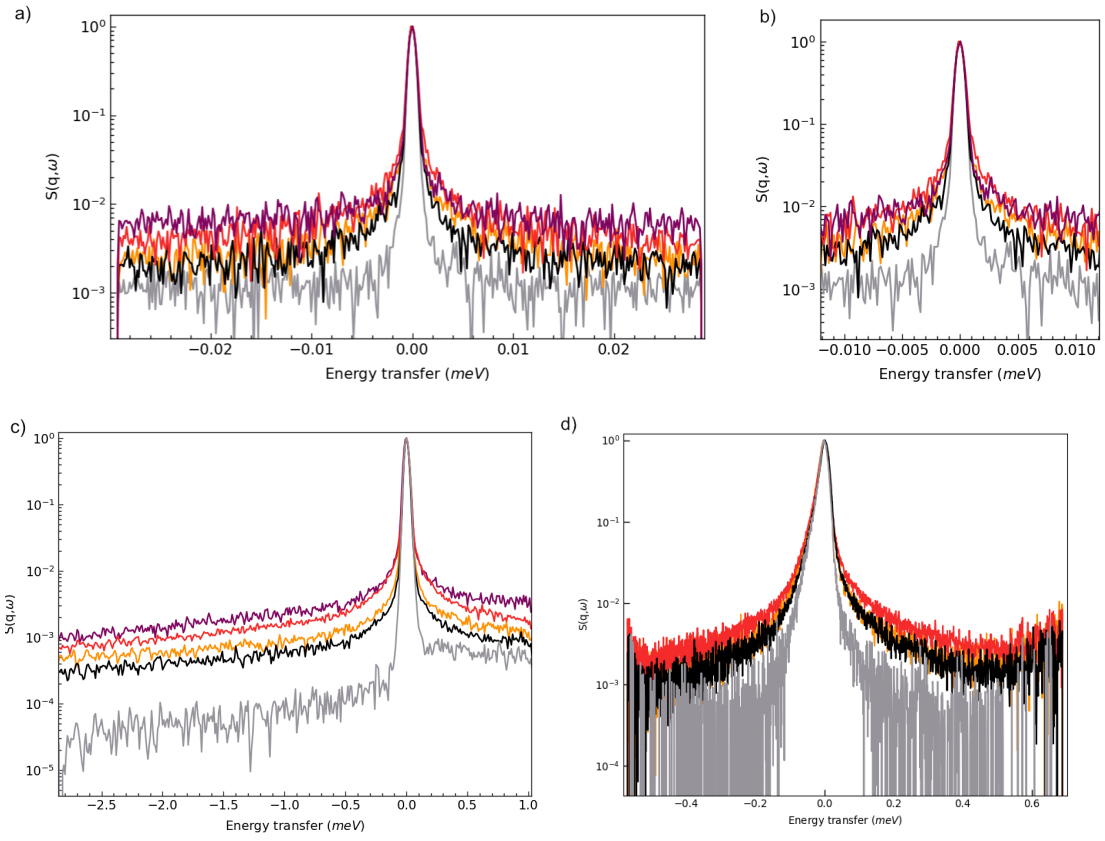

Figure 4.21: a) QENS spectra from IN16b at $q = 0.95$ Å^{-1}, normalized to the elastic value for AX0.9 (black) and DiolAX25 (orange), BGE-AX0.9 (purple) and BGE-DiolAX0.9 kept at 53% RH (D_2O), and b) zoomed in data around the elastic line. c) shows data treated the same way for SHARPER at $q = 0.98$ Å^{-1}, and d) for OSIRIS at $q = 1.08$ Å^{-1}. The grey spectra shows the resolution function, and errors have been omitted for visibility.

Dynamics at longer time-scales

DMA data at a frequency of 1 Hz for a compression molded BGE-DiolAX0.9 film is shown in Figure 4.22, adapted from data in paper IV. From the data, three different transitions were observed. We refer to them in order of increasing temperature as the γ, β and α transitions. The γ transition occurred at ca. -90 °C, the β transition at ca. -50 °C and the α at approx. 70 °C. After the β transition, E' decreased by more than one order of magnitude. Beyond the α transition at 70 °C, both E' and E'' decreases even further, at which point it was possible to compression mold the sample. Compared to unmodified AX in Figure 4.13, the E' of BGE-DiolAX0.9 at 100 °C is lower by about two orders of magnitude.

The results reported in this work, and in previous work by Deralia et al. [108], indicate that the addition of BGE creates transitions below 0 °C. The β transition is therefore likely attributed to the relaxation of the side chains, this is in agreement with works on cellulose esters [52] and glucomannan esters [54] where a relaxation around -60 °C was observed. The presence of a γ transition in our systems also suggests that BGE-DiolAX sidechains contribute with additional modes of movement. Lastly, the α transition is attributed to relaxations of the AX main chain.

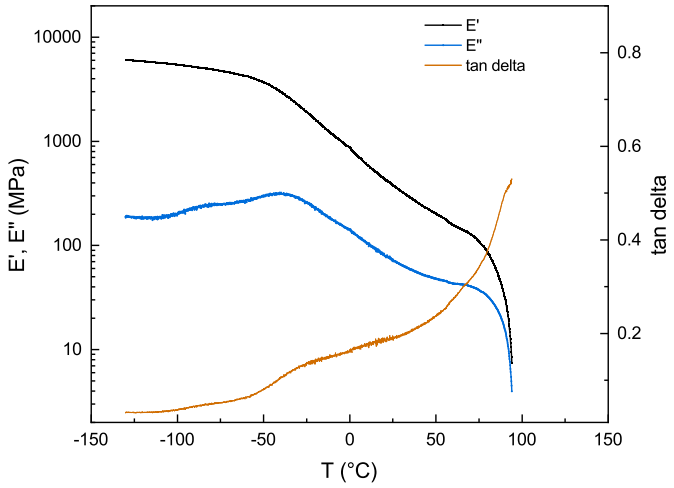

Figure 4.22: E', E'' and tan delta of a compression molded BGE-DiolAX0.9 film collected at a frequency of 1 Hz, amplitude of 8 µm (approximately 0.05% strain), and heating rate of 3 °C · min^{-1}. Adapted from Janewithayapun, R. et al., *Carbohydrate Polymers*, 2024 under the CC-BY license.

For comparison, DMA was measured under the same conditions for BGE-AX0.9, shown in Figure 4.23 (lowest test temperature slightly higher due to chiller limitations). In comparison to BGE-DiolAX0.9, we observe a smaller decrease in E' from -50 °C upwards, and no clear peaks in either E'' or tan delta could be observed. It is only when the main chain α transition is reached that the material softens by more than one order of magnitude. The onset of the α transition is also shifted upwards to 100 °C compared to approximately 70 °C for BGE-DiolAX0.9. The observations by DMA corroborates well with the FWS data from QENS. The side chain dynamics do not contribute as much

to chain mobility in BGE-AX0.9, and the main chain dynamics are not as prominent until a higher temperature.

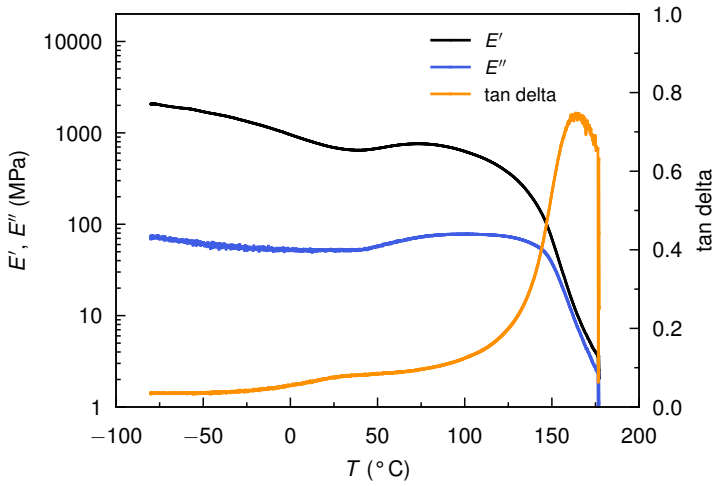

Figure 4.23: E', E'' and tan delta of a compression molded BGE-AX0.9 film collected at a frequency of 1 Hz, amplitude of 0.05 % strain, and heating rate of 3 °C · min^{-1}.

Etherification contributes strongly to thermoplasticity in AX by adding subglass transition dynamics that increase the mobility of the material. We observe from both QENS and DMA that prior ring-opening of AX, despite modifying mainly the arabinose units, result in higher mobility of not only the DiolAX main chain, but also of the added BGE ether segments.

4.7 Processability of etherified ring-opened arabinoxylan materials

This section is a short summary of the knowledge and insights gained on the processability of AX derivatives during my PhD. The processing aspect has not been a major focus of my project and the results here are presented in case some of the observations prove useful to other researchers.

From results in Section 4.6, the most straightforward method to produce a melt processable AX material would be to perform an etherification directly on the material. Due to the effects of A/X ratio on AX properties, it is likely that a highly branched AX such as AX0.9 would perform better. This is because these fractions are more water soluble, as shown in paper I, hence the etherification is expected to be more effective. In paper IV, it was also shown that AX0.9 resulted in the material with the lowest E' as a function of temperature. Compared to a material that is both ring-opened and etherified such as BGE-DiolAX0.9, a BGE-AX0.9 will however, be less flexible at room temperature, which we attribute to differences in the dynamics on the molecular scale.

The compression molding temperature window of a BGE-DiolAX material (BGE-DiolAX0.3 from paper IV) has also been investigated. The material was cut into small pieces and compression molded at different temperatures. At approximately 60 °C, the pieces were not melted during the process (Figure 4.24a), while above the α transition (Figure 4.22), here at 90 °C, a complete film was formed (Figure 4.24b).

While all tested BGE-DiolAX materials begin to show degradation at 200 °C under N_2 atmosphere, when heated in air, discoloration occurs around 150 °C. This provides a rough estimate of the upper limit of the processing window for these materials. Processing above this temperature has been attempted during extrusion.

The second batch of BGE-DiolAX0.9 had a lower BGE DS than 1, based on ^{1}H NMR comparisons. This material was compression moldable with the same conditions at 140 °C, showing that the BGE content required for melt processability is lower than DS 1.0. Calculating based on the molar mass of BGE (130 $g \cdot mol^{-1}$) and that of one AX monomer repeating unit (132 $g \cdot mol^{-1}$), this BGE-DiolAX0.9 consists of more than 50% polysaccharide by mass, signifying a step towards a more commercially viable modified natural polymer material.

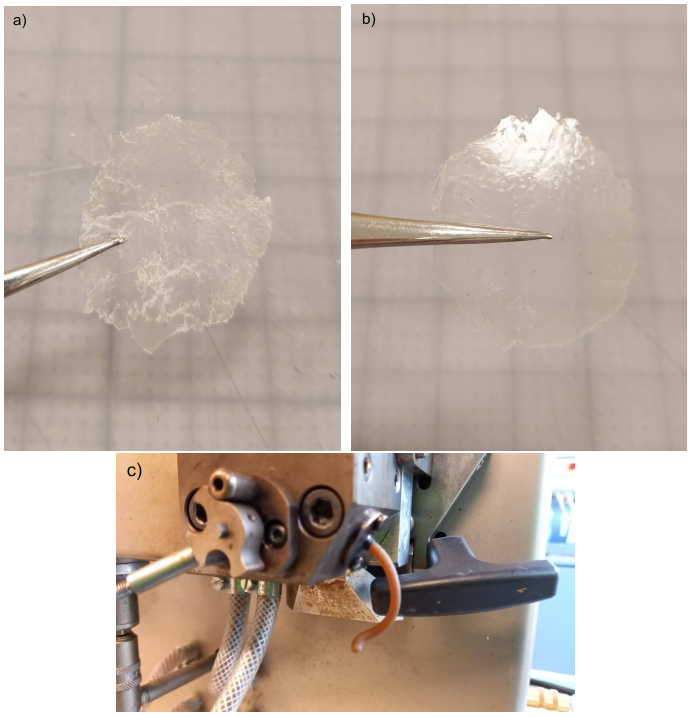

Figure 4.24: BGE-DiolAX0.3 melt compressed at 60 °C a) and 90 °C b), both were compression molded at 50 kN force for 3 min. c) Extruded filament of BGE-DiolAX

Experiments with melt extrusion show that it is indeed possible to extrude BGE-DiolAX materials. A 10 g batch of BGE-DiolAX with DO of 30% and BGE DS of 1.2 was prepared and sent to collaborators where extrusion was performed at 160 °C with a microcompounder (Figure 4.24c). The extruded filaments were brown in color, likely a mix of the material's original color (slightly brown

when thickness above 1 mm) and of discoloration from degradation during processing.

Chapter 5

Concluding remarks and outlook

The overarching goal of thesis has been to further our understanding of the mechanisms by which chemical modification of polysaccharides improve their melt processability and bulk properties, so that future development of modification routes can be better predicted.

In the structural aspect of the materials, the conformation of AX in water dispersions vary with their chemical composition. More substituted AX having a longer persistence length and interacting more favorably with water. When AX is modified with periodate oxidation and borohydride reduction to achieve ring-opening of the polysaccharide, the conformation of dialcohol AX in dispersion does not significantly change. The chain persistence length of the most modified dialcohol AX is 10% lower than AX, a negligible decrease compared to the 300% reduction observed in alginate [45]. It is instead the inter-molecular interactions that vary, first becoming increasingly attractive with periodate oxidation to dialdehyde AX, and subsequently reverting to being repulsive after reduction to dialcohol AX. It was revealed that it is predominantly the arabinose side-groups that are modified by ring-opening modification. The xylan backbone of AX was therefore, not modified to the same extent as would occur when oxidizing linear polysaccharides. This explains why the conformation changes observed in oxidized cellulose or alginate, are less pronounced in AX.

On the other hand, we observed changes in the dynamics of the ring-opened materials at 10% wt. moisture content. The chain mobility of ring-opened arabinoxylan was shown to increase and we could further assign the increased motions to the ring-opened C2 and C3 sites. Moreover, the dynamics in ring-opened dialcohol AX is more strongly plasticized by water than AX or dialdehyde AX.

The last step of the modification route studied in this thesis was the etherification with BGE. The addition of the BGE side chains result in nano-phase separation of the system into side chain rich and DiolAX/AX domains. The size of the nano-domains are affected by the chemical composition of the starting AX material and by the crystallinity in AX, which occurs at low

substitution ratios. The properties of the AX starting material also affects the stiffness and ductility of the derivatized BGE-DiolAX material.

As a result of the nano-phase separation, the BGE-DiolAX material exhibits two glass transition temperatures (T_g), a side chain T_g and a main chain $T_{g,\alpha}$. In BGE-DiolAX, the main chain, i.e. the DiolAX segment, behaves similarly to that of DiolAX, while the BGE side chains have motions at even faster correlation times. The BGE-DiolAX was also compared with BGE-AX, which was etherified without prior ring-opening. The overall number of motions in the two materials as a function of temperature were the same, consisting of side chain motions with onset below 0 °C, and a main chain motion with onset above 0 °C. However, both motions in BGE-DiolAX contributed to larger changes in stiffness with temperature. The relaxations of both the side chain and main chain appears less intense or occurs at higher temperatures for BGE-AX. The comparison indicates therefore, a benefit on the mobility of the main chain and the BGE side chain from the ring-opening modification steps prior to etherification.

For future work, investigations should focus on the impact of the ring-opening of the arabinose side-groups on the molecular motions of the chain. It would also be interesting to confirm the hypothesis that ring-opening results in higher mobility of the grafted BGE side chains. Lastly, it would be of larger practical applicability if the conclusion made in this work could be tested in other polysaccharides and with other chemical modification routes based on the same principle. If softening the polysaccharide main chain prior to the addition of flexible side chains does indeed provide a synergistic effect, the method could be useful as a general blueprint for designing thermoplastic polysaccharide materials.

Bibliography

(1) Schooneveld-Bergmans, M.; Beldman, G.; Voragen, A. *Journal of Cereal Science* **1999**, *29*, 63–75 (cit. on p. 3).

(2) Ebringerová, A.; Hromádková, Z.; Heinze, T. *Polysaccharides I: Structure, characterization and use* **2005**, 1–67 (cit. on pp. 3, 5).

(3) Of Agriculture, U. S. D. Wheat Explorer - Global Wheat Data, `https://ipad.fas.usda.gov/cropexplorer/cropview/commodityView.aspx?cropid=0410000`, Accessed: 2025-08-06, 2025 (cit. on p. 3).

(4) Marcotuli, I.; Hsieh, Y. S.-Y.; Lahnstein, J.; Yap, K.; Burton, R. A.; Blanco, A.; Fincher, G. B.; Gadaleta, A. *Journal of agricultural and food chemistry* **2016**, *64*, 2883–2892 (cit. on p. 3).

(5) Saulnier, L.; Sado, P.-E.; Branlard, G.; Charmet, G.; Guillon, F. *Journal of Cereal Science* **2007**, *46*, 261–281 (cit. on p. 3).

(6) Santibáñez, L.; Henríquez, C.; Corro-Tejeda, R.; Bernal, S.; Armijo, B.; Salazar, O. *Carbohydrate Polymers* **2021**, *251*, 117118 (cit. on p. 3).

(7) Apprich, S.; Tirpanalan, Ö.; Hell, J.; Reisinger, M.; Böhmdorfer, S.; Siebenhandl-Ehn, S.; Novalin, S.; Kneifel, W. *LWT-Food Science and Technology* **2014**, *56*, 222–231 (cit. on pp. 3, 5).

(8) Börjesson, M.; Westman, G.; Larsson, A.; Ström, A. *ACS Applied Polymer Materials* **2019**, *1*, 1443–1450 (cit. on pp. 3, 7).

(9) Farhat, W.; Venditti, R.; Ayoub, A.; Prochazka, F.; Fernández-de Alba, C.; Mignard, N.; Taha, M.; Becquart, F. *Materials & Design* **2018**, *153*, 298–307 (cit. on p. 3).

(10) Janewithayapun, R.; Hedenqvist, M. S.; Cousin, F.; Idström, A.; Evenäs, L.; Lopez-Sanchez, P.; Westman, G.; Larsson, A.; Ström, A. *Carbohydrate Polymers* **2024**, *331*, 121846 (cit. on pp. 3, 38–40, 45, 50).

(11) Fundador, N. G. V.; Enomoto-Rogers, Y.; Takemura, A.; Iwata, T. *Polymer* **2012**, *53*, 3885–3893 (cit. on pp. 3, 7).

(12) Sandberg, A.-S.; Andersson, H.; Hallgren, B.; Hasselblad, K.; Isaksson, B.; Hultén, L. *British Journal of Nutrition* **1981**, *45*, 283–294 (cit. on p. 5).

(13) Ek, M.; Gellerstedt, G.; Henriksson, G., *Volume 1 Wood Chemistry and Wood Biotechnology*; De Gruyter: Berlin, New York, 2009 (cit. on p. 5).

(14) Schooneveld-Bergmans, M.; Beldman, G; Voragen, A. *Journal of Cereal Science* **1999**, *29*, 63–75 (cit. on pp. 5, 6).

(15) De Man, W. L.; Vaneeckhaute, E.; De Brier, N.; Wouters, A. G.; Martens, J. A.; Breynaert, E.; Delcour, J. A. *Journal of Agricultural and Food Chemistry* **2021**, *69*, 3912–3922 (cit. on pp. 5, 6).

(16) Pietiäinen, S.; Moldin, A.; Ström, A.; Malmberg, C.; Langton, M. *Food Chemistry* **2022**, *383*, 132584 (cit. on p. 5).

(17) Brillouet, J.-M.; Joseleau, J.-P. *Carbohydrate Research* **1987**, *159*, 109–126 (cit. on p. 6).

(18) Bacic, A.; Stone, B. A. *Functional Plant Biology* **1981**, *8*, 475–495 (cit. on p. 6).

(19) Pitkänen, L.; Tuomainen, P.; Virkki, L.; Tenkanen, M. *International Journal of Biological Macromolecules* **2011**, *49*, 963–969 (cit. on p. 6).

(20) Köhnke, T.; Östlund, Å.; Brelid, H. *Biomacromolecules* **2011**, *12*, 2633–2641 (cit. on pp. 6, 28, 30).

(21) Andrewartha, K. A.; Phillips, D. R.; Stone, B. A. *Carbohydrate Research* **1979**, *77*, 191–204 (cit. on pp. 6, 11, 28, 30, 35).

(22) Pitkänen, L.; Virkki, L.; Tenkanen, M.; Tuomainen, P. *Biomacromolecules* **2009**, *10*, 1962–1969 (cit. on pp. 6, 11).

(23) Dervilly-Pinel, G.; Thibault, J.-F.; Saulnier, L. *Carbohydrate Research* **2001**, *330*, 365–372 (cit. on pp. 6, 11).

(24) Picout, D. R.; Ross-Murphy, S. B. *Carbohydrate Research* **2002**, *337*, 1781–1784 (cit. on pp. 6, 11).

(25) Petermann, M.; Dianteill, L.; Zeidi, A.; Vaha Ouloassekpa, R.; Budisavljevic, P.; Le Men, C.; Montanier, C.; Roblin, P.; Cabane, B.; Schweins, R.; Dumon, C.; Bouchoux, A. *Biomacromolecules* **2023**, *24*, 3619–3628 (cit. on pp. 6, 11, 12).

(26) Höije, A.; Sternemalm, E.; Heikkinen, S.; Tenkanen, M.; Gatenholm, P. *Biomacromolecules* **2008**, *9*, 2042–2047 (cit. on p. 6).

(27) Heikkinen, S. L.; Mikkonen, K. S.; Pirkkalainen, K.; Serimaa, R.; Joly, C.; Tenkanen, M. *Carbohydrate Polymers* **2013**, *92*, 733–740 (cit. on pp. 6, 12, 13, 37, 38).

(28) DRYHURST, G. In *Periodate Oxidation of Diol and Other Functional Groups*, DRYHURST, G., Ed.; Pergamon: 1970, pp 3–16 (cit. on p. 6).

(29) Simon, J.; Fliri, L.; Drexler, F.; Bacher, M.; Sapkota, J.; Ristolainen, M.; Hummel, M.; Potthast, A.; Rosenau, T. *Carbohydrate Polymers* **2023**, *310*, 120691 (cit. on p. 6).

(30) Buist, G.; Bunton, C.; Miles, J. *Journal of the Chemical Society (Resumed)* **1959**, 743–748 (cit. on p. 6).

(31) Buist, G.; Bunton, C.; Hipperson, W. *Journal of the Chemical Society B: Physical Organic* **1971**, 2128–2142 (cit. on p. 6).

(32) Painter, T. J. *Carbohydrate Research* **1988**, *179*, 259–268 (cit. on pp. 6, 7, 21, 34).

(33) Palasingh, C.; Ström, A.; Amer, H.; Nypelö, T. *International Journal of Biological Macromolecules* **2021**, *180*, 753–759 (cit. on p. 7).

(34) Amer, H.; Nypelö, T.; Sulaeva, I.; Bacher, M.; Henniges, U.; Potthast, A.; Rosenau, T. *Biomacromolecules* **2016**, *17*, 2972–2980 (cit. on p. 7).

(35) Münster, L.; Vícha, J.; Klofáč, J.; Masař, M.; Kucharczyk, P.; Kuřitka, I. *Cellulose* **2017**, *24*, 2753–2766 (cit. on pp. 7, 31).

(36) Larsson, P. A.; Gimåker, M.; Wågberg, L. *Cellulose* **2008**, *15*, 837–847 (cit. on p. 7).

(37) Larsson, P. A.; Berglund, L. A.; Wågberg, L. *Biomacromolecules* **2014**, *15*, 2218–2223 (cit. on p. 7).

(38) Chemin, M.; Rakotovelo, A.; Ham-Pichavant, F.; Chollet, G.; da Silva Perez, D.; Petit-Conil, M.; Cramail, H.; Grelier, S. *Holzforschung* **2015**, *69*, 713–720 (cit. on p. 7).

(39) Simon, J.; Fliri, L.; Sapkota, J.; Ristolainen, M.; Miller, S. A.; Hummel, M.; Rosenau, T.; Potthast, A. *Biomacromolecules* **2023**, *24*, 166–177 (cit. on p. 7).

(40) Esen, E.; Meier, M. A. R. *ACS Sustainable Chemistry & Engineering* **2020**, *8*, 15755–15760 (cit. on p. 7).

(41) Kristiansen, K. A.; Potthast, A.; Christensen, B. E. *Carbohydrate Research* **2010**, *345*, Special Issue: Selected Papers from the 15th European Carbohydrate Symposium, Vienna 2009, 1264–1271 (cit. on p. 7).

(42) Börjesson, M.; Larsson, A.; Westman, G.; Ström, A. *Carbohydrate Polymers* **2018**, *202*, 280–287 (cit. on pp. 7, 40).

(43) Simon, J.; Schlapp-Hackl, I.; Sapkota, J.; Ristolainen, M.; Rosenau, T.; Potthast, A. *ChemSusChem* **2024**, *17*, e202300791 (cit. on p. 7).

(44) Potthast, A.; Kostic, M.; Schiehser, S.; Kosma, P.; Rosenau, T. *Holzforschung* **2007**, *61*, 662–667 (cit. on pp. 7, 32, 36).

(45) Vold, I. M. N.; Kristiansen, K. A.; Christensen, B. E. *Biomacromolecules* **2006**, *7*, 2136–2146 (cit. on pp. 7, 32, 55).

(46) Christensen, B. E.; Vold, I. M. N.; Vårum, K. M. *Carbohydrate Polymers* **2008**, *74*, 559–565 (cit. on p. 7).

(47) Morooka, T.; Norimoto, M.; Yamada, T. *Journal of Applied Polymer Science* **1989**, *38*, 849–858 (cit. on p. 7).

(48) Pellegrino, E.; Al-Rudainy, B.; Larsson, P. A.; Fina, A.; Lo Re, G. *Carbohydrate Polymer Technologies and Applications* **2025**, *9*, 100642 (cit. on p. 7).

(49) Börjesson, M.; Larsson, A.; Westman, G.; Ström, A. A process for preparing modified hemicellulose, EP3700941A1·2020-09-02, Accessed: 2023-10-14, 2018 (cit. on p. 7).

(50) Börjesson, M.; Westman, G.; Larsson, A.; Ström, A. *ACS Applied Polymer Materials* **2019**, *1*, 1443–1450 (cit. on pp. 7, 8).

(51) Deralia, P. K.; du Poset, A. M.; Lund, A.; Larsson, A.; Ström, A.; Westman, G. *International Journal of Biological Macromolecules* **2021**, *188*, 491–500 (cit. on p. 7).

(52) Crépy, L.; Miri, V.; Joly, N.; Martin, P.; Lefebvre, J.-M. *Carbohydrate polymers* **2011**, *83*, 1812–1820 (cit. on pp. 7, 40, 50).

(53) Liu, L.; Lyu, D.; Xiang, M.; Men, Y. *Polymer Crystallization* **2020**, *3*, e10110 (cit. on p. 7).

(54) Enomoto-Rogers, Y.; Ohmomo, Y.; Takemura, A.; Iwata, T. *Carbohydrate Polymers* **2014**, *101*, 592–599 (cit. on pp. 7, 8, 50).

(55) Dervilly, G.; Saulnier, L; Roger, P; Thibault, J.-F. *Journal of Agricultural and Food Chemistry* **2000**, *48*, 270–278 (cit. on p. 11).

(56) Muller, F.; Manet, S.; Jean, B.; Chambat, G.; Boué, F.; Heux, L.; Cousin, F. *Biomacromolecules* **2011**, *12*, 3330–3336 (cit. on pp. 11, 12, 28).

(57) Beaucage, G.; Rane, S.; Sukumaran, S.; Satkowski, M. M.; Schechtman, L. A.; Doi, Y. *Macromolecules* **1997**, *30*, 4158–4162 (cit. on pp. 11, 28).

(58) Hammouda, B The SANS toolbox, 2008 (cit. on p. 11).

(59) Rubinstein, M.; Colby, R. H., *Polymer Physics*; Oxford University Press: 2003, pp 97–126 (cit. on pp. 11, 28).

(60) Pedersen, J. S.; Schurtenberger, P. *Macromolecules* **1996**, *29*, 7602–7612 (cit. on pp. 11, 24, 28).

(61) Yu, L.; Yakubov, G. E.; Martínez-Sanz, M.; Gilbert, E. P.; Stokes, J. R. *Carbohydrate Polymers* **2018**, *193*, 179–188 (cit. on p. 11).

(62) Pedersen, J. S.; Schurtenberger, P. *Journal of Polymer Science Part B: Polymer Physics* **2004**, *42*, 3081–3094 (cit. on pp. 12, 24, 29).

(63) Schönhals, A.; Kremer, F. In *Polymer Science: A Comprehensive Reference*, Matyjaszewski, K., Möller, M., Eds.; Elsevier: Amsterdam, 2012, pp 296–297 (cit. on pp. 12, 37).

(64) Nieduszynski, I.; Marchessault, R. *Biopolymers: Original Research on Biomolecules* **1972**, *11*, 1335–1344 (cit. on p. 12).

(65) Gabbay, S.; Sundararajan, P.; Marchessault, R. *Biopolymers: Original Research on Biomolecules* **1972**, *11*, 79–94 (cit. on p. 12).

(66) Marchessault, R.; Settineri, W. *Journal of Polymer Science Part B: Polymer Letters* **1964**, *2*, 1047–1051 (cit. on p. 12).

(67) Yui, T.; Imada, K.; Shibuya, N.; Ogawa, K. *Bioscience, biotechnology, and biochemistry* **1995**, *59*, 965–968 (cit. on p. 12).

(68) Lelliott, C; Atkins, E.; Juritz, J.; Stephen, A. *Polymer* **1978**, *19*, 363–367 (cit. on p. 12).

(69) Mikkonen, K. S.; Pitkänen, L.; Liljeström, V.; Mabasa Bergström, E.; Serimaa, R.; Salmén, L.; Tenkanen, M. *Cellulose* **2012**, *19*, 467–480 (cit. on p. 12).

(70) Beiner, M.; Huth, H. *Nature materials* **2003**, *2*, 595–599 (cit. on pp. 12, 13).

(71) Miller, R. L.; Boyer, R. F.; Heijboer, J *Journal of Polymer Science: Polymer Physics Edition* **1984**, *22*, 2021–2041 (cit. on p. 12).

(72) Rottler, J.; Robbins, M. O. *Physical Review E* **2003**, *68*, 011801 (cit. on pp. 12, 37).

(73) Gedde, U. W.; Hedenqvist, M. S.; Hakkarainen, M.; Nilsson, F.; Das, O. In *Applied Polymer Science*; Springer International Publishing: Cham, 2021, pp 1–60 (cit. on p. 14).

(74) Mirau, P. A. In *A Practical Guide to Understanding the NMR of Polymers*; John Wiley & Sons: 2004, pp 359–396 (cit. on pp. 14–17, 43).

(75) McBrierty, V. J.; Packer, K. J. In *Nuclear Magnetic Resonance in Solid Polymers*; Cambridge Solid State Science Series; Cambridge University Press: 1993, 16–50 (cit. on pp. 15, 43).

(76) Hartmann, S. R.; Hahn, E. L. *Phys. Rev.* **1962**, *128*, 2042–2053 (cit. on p. 15).

(77) Lindberg, J. J.; Hortling, B. In *Characterization of Polymers in the Solid State I: Part A: NMR and Other Spectroscopic Methods Part B: Mechanical Methods*, ed. by Kaush, H. H.; Zachman, H. G., Springer Berlin Heidelberg: Berlin, Heidelberg, 1985, pp 1–22 (cit. on p. 15).

(78) Mirau, P. A. In *A Practical Guide to Understanding the NMR of Polymers*; John Wiley & Sons: 2004, pp 66–77 (cit. on p. 16).

(79) Khashami, F. In *Fundamentals of NMR and MRI: From Quantum Principles to Medical Applications*; Springer Nature Switzerland: Cham, 2024, pp 91–106 (cit. on p. 16).

(80) McBrierty, V. J. In *Comprehensive Polymer Science: The Synthesis, Characterization, Reactions & Applications of Polymers*, Allen, G., Bevington, J. C., Eds.; Pergamon Press: Oxford, 1989; Vol. 1; Chapter 19 (cit. on p. 16).

(81) Heatley, F. In *Comprehensive Polymer Science: The Synthesis, Characterization, Reactions & Applications of Polymers*, Allen, G., Bevington, J. C., Eds.; Pergamon Press: Oxford, 1989; Vol. 1; Chapter 18 (cit. on p. 16).

(82) Schmidt-Rohr, K.; Clauss, J.; Spiess, H. W. *Macromolecules* **1992**, *25*, 3273–3277 (cit. on pp. 17, 18, 43).

(83) Radloff, D.; Boeffel, C.; Spiess, H. W. *Macromolecules* **1996**, *29*, 1528–1534 (cit. on pp. 17, 43).

(84) Gerstl, C.; Schneider, G. J.; Fuxman, A.; Zamponi, M.; Frick, B.; Seydel, T.; Koza, M.; Genix, A. C.; Allgaier, J.; Richter, D.; Colmenero, J.; Arbe, A. *Macromolecules* **2012**, *45*, 4394–4405 (cit. on pp. 18, 19).

(85) Newport, R.; Rainford, B.; Cywinski, R. In Adam Hilger.: 1988; Chapter 17 (cit. on p. 18).

(86) Berrod, Quentin; Lagrené, Karine; Ollivier, Jacques; Zanotti, Jean-Marc *EPJ Web of Conferences* **2018**, *188*, 05001 (cit. on p. 18).

(87) Arrighi, V.; Ferguson, R.; Lechner, R.; Telling, M.; Triolo, A. *Physica B: Condensed Matter* **2001**, *301*, Proceedings of the Fifth International Workshop on Quasi-Elastic Neutron Scattering, 35–43 (cit. on pp. 18–20).

(88) Frick, B.; Combet, J.; van Eijck, L. *Nuclear Instruments and Methods in Physics Research Section A: Accelerators, Spectrometers, Detectors and Associated Equipment* **2012**, *669*, 7–13 (cit. on pp. 19, 20, 44, 45, 48).

(89) Jensen, A. B.; Christensen, T. E. K.; Weninger, C.; Birkedal, H. *Journal of Synchrotron Radiation* **2022**, *29*, 1420–1428 (cit. on p. 23).

(90) Hammouda, B. In *Polymer Characteristics*; Springer Berlin Heidelberg: Berlin, Heidelberg, 1993, pp 87–133 (cit. on p. 24).

(91) Pedersen, J. S.; Svaneborg, C. *Current Opinion in Colloid & Interface Science* **2002**, *7*, 158–166 (cit. on p. 24).

(92) Westberry, B. P.; Mansel, B. W.; Ryan, T. M.; Lundin, L.; Williams, M. *Carbohydrate Polymers* **2022**, *296*, 119958 (cit. on p. 24).

(93) Debye, P. *The Journal of Physical and Colloid Chemistry* **1947**, *51*, 18–32 (cit. on p. 24).

(94) Janewithayapun, R.; Cousin, F.; de Moura Pereira, P. F.; Herranz-Trillo, F.; Terry, A. E.; Pedersen, J. S.; Jiménez-Quero, A.; Ström, A. *Carbohydrate Polymers* **2025**, *368*, 124082 (cit. on pp. 27, 29–31).

(95) Glatter, O. In Academic Press: 1982; Chapter 11, pp 363–385 (cit. on p. 28).

(96) Thompson, C. J.; Ryan, A. J. In *Neutrons, X-rays, and Light (Second Edition)*, Lindner, P., Oberdisse, J., Eds., Second Edition; Elsevier: 2025, pp 285–310 (cit. on p. 29).

(97) Lindner, P. In *Neutrons, X-rays and light: Scattering methods applied to soft condensed matter*; Elsevier: 2002, pp 23–48 (cit. on p. 29).

(98) Veelaert, S.; de Wit, D.; Gotlieb, K.; Verhé, R. *Carbohydrate Polymers* **1997**, *32*, 131–139 (cit. on p. 31).

(99) Yao, H.; Wang, Y.; Yin, J.; Nie, S.; Xie, M. *Molecules* **2021**, *26* (cit. on p. 33).

(100) De Man, W. L.; Chandran, C. V.; Wouters, A. G.; Radhakrishnan, S.; Martens, J. A.; Breynaert, E.; Delcour, J. A. *Journal of Agricultural and Food Chemistry* **2022**, *70*, 10604–10610 (cit. on p. 33).

(101) Simon, J.; Fliri, L.; Fröhlich, F.; Sapkota, J.; Ristolainen, M.; Hummel, M.; Rosenau, T.; Potthast, A. *Cellulose* **2023**, *30*, 8205–8220 (cit. on p. 34).

(102) Vold, I. M. N.; Kristiansen, K. A.; Christensen, B. E. *Biomacromolecules* **2006**, *7*, 2136–2146 (cit. on p. 36).

(103) Brown, H. R. *Materials Science Reports* **1987**, *2*, 317–370 (cit. on p. 37).

(104) Paredes, E.; Fischer, E. W. *Die Makromolekulare Chemie: Macromolecular Chemistry and Physics* **1979**, *180*, 2707–2722 (cit. on p. 37).

(105) Hiller, S; Pascui, O; Budde, H; Kabisch, O; Reichert, D; Beiner, M *New Journal of Physics* **2004**, *6*, 10 (cit. on p. 39).

(106) Hodge, R. M.; Bastow, T. J.; Edward, G. H.; Simon, G. P.; Hill, A. J. *Macromolecules* **1996**, *29*, 8137–8143 (cit. on p. 43).

(107) Teixeira, J.; Bellissent-Funel, M.-C.; Chen, S. H.; Dianoux, A. J. *Phys. Rev. A* **1985**, *31*, 1913–1917 (cit. on p. 45).

(108) Deralia, P. K.; Sonker, A. K.; Lund, A.; Larsson, A.; Ström, A.; Westman, G. *Chemosphere* **2022**, *294*, 133618 (cit. on p. 50).